

# A physical model for cosmological simulations of galaxy formation: multi-epoch validation

Paul Torrey<sup>1\*</sup>, Mark Vogelsberger<sup>1†</sup>, Shy Genel<sup>1</sup>, Debora Sijacki<sup>2</sup>, Volker Springel<sup>3,4</sup> and Lars Hernquist<sup>1</sup>

<sup>1</sup> *Harvard-Smithsonian Center for Astrophysics, 60 Garden Street, Cambridge, MA, 02138, USA*

<sup>2</sup> *Institute of Astronomy and Kavli Institute for Cosmology, University of Cambridge, Madingley Road, Cambridge CB3 0HA*

<sup>3</sup> *Heidelberg Institute for Theoretical Studies, Schloss-Wolfsbrunnengasse 35, 69118 Heidelberg, Germany*

<sup>4</sup> *Zentrum für Astronomie der Universität Heidelberg, ARI, Mönchhofstr. 12-14, 69120 Heidelberg, Germany*

5 August 2018

## ABSTRACT

We present a multi-epoch analysis of the galaxy populations formed within the cosmological hydrodynamical simulations presented in Vogelsberger et al. (2013). These simulations explore the performance of a recently implemented feedback model which includes primordial and metal line radiative cooling with self-shielding corrections; stellar evolution with associated mass loss and chemical enrichment; feedback by stellar winds; black hole seeding, growth and merging; and AGN quasar- and radio-mode heating with a phenomenological prescription for AGN electro-magnetic feedback. We illustrate the impact of the model parameter choices on the resulting simulated galaxy population properties at high and intermediate redshifts. We demonstrate that our scheme is capable of producing galaxy populations that broadly reproduce the observed galaxy stellar mass function extending from redshift  $z = 0$  to  $z = 3$ . We also characterise the evolving galactic B-band luminosity function, stellar mass to halo mass ratio, star formation main sequence, Tully-Fisher relation, and gas-phase mass-metallicity relation and confront them against recent observational estimates. This detailed comparison allows us to validate elements of our feedback model, while also identifying areas of tension that will be addressed in future work.

**Key words:** methods: numerical – cosmology: theory – cosmology: galaxy formation

## 1 INTRODUCTION

Cosmological simulations are among the most powerful tools available for studying the non-linear regime of cosmic structure formation. While dark matter only simulations have built a solid foundation for our understanding of the origin of haloes via gravitational collapse (e.g., Springel et al. 2005c; Boylan-Kolchin et al. 2009; Fosalba et al. 2008; Teyssier et al. 2009; Klypin et al. 2011), applying their findings to our understanding of the observable Universe (i.e. luminous galaxies) requires modelling of baryonic physics as well. Although semi-analytic (e.g., White & Frenk 1991; Kauffmann et al. 1999; Hatton et al. 2003; Kang et al. 2005; Somerville et al. 2008; Guo et al. 2011, 2012) and halo occupation distribution (e.g., Vale & Ostriker 2004; Conroy et al. 2006;

Behroozi et al. 2012; Moster et al. 2012) models can estimate galaxy properties based on dark matter only simulations, the most direct and self-consistent way to explore the evolution of observable galaxies theoretically is by including baryons in the simulations (e.g. Katz et al. 1992, 1996; Weinberg et al. 1997; Murali et al. 2002; Springel & Hernquist 2003b; Kereš et al. 2005; Ocvirk et al. 2008; Crain et al. 2009; Croft et al. 2009; Schaye et al. 2010; Oppenheimer et al. 2010; Vogelsberger et al. 2012).

The main challenge for any large-scale galaxy formation model is accurately handling the baryonic physics and including proper forms of feedback to regulate star formation. Galaxy formation simulations lacking strong feedback substantially overproduce stars, leading to galaxies with too high baryon fractions (e.g., White & Frenk 1991; Balogh et al. 2001; Scannapieco et al. 2012). This problem is most pronounced for the highest and lowest mass systems, where star formation is known to be relatively inefficient (e.g.,

\* E-mail: ptorrey@cfa.harvard.edu

† Hubble Fellow.

Behroozi et al. 2012, and references therein). The problem can be remedied by introducing sources of feedback which either eject gas from galaxies or heat it to prevent continued accretion from the halo. Two commonly employed strong feedback mechanisms are star formation (Dekel & Silk 1986; Thacker & Couchman 2000; Springel & Hernquist 2003a; Kawata & Gibson 2003; Stinson et al. 2006; Scannapieco et al. 2008; Dalla Vecchia & Schaye 2008; Okamoto et al. 2010; Stinson et al. 2013) and black hole growth (Springel et al. 2005b; Kawata & Gibson 2005; Di Matteo et al. 2005; Thacker et al. 2006; Sijacki et al. 2007; Okamoto et al. 2008; Kurosawa & Proga 2009; Booth & Schaye 2009; Debuhr et al. 2011; Dubois et al. 2012).

Winds driven by star formation are a consequence of energy and/or momentum injection from newly formed stellar populations into the interstellar medium (ISM). Observations indicate that star forming galaxies show signs of outflowing material (e.g., Heckman et al. 2000; Rupke et al. 2002, 2005), and that the velocity of the outflowing wind material may scale with the mass of the galaxy (Martin 2005). Including winds in large-scale cosmological simulations requires sub-grid models because the detailed ISM structure remains unresolved (Hopkins et al. 2012a, 2013a,b). Several types of explicit wind models have been developed including hydrodynamically decoupled winds (Springel & Hernquist 2003a), injecting thermal energy while shutting down cooling (Stinson et al. 2006, 2013), or adding blast particles to launch a Sedov-Taylor blast wave (Dubois & Teyssier 2008). These wind prescriptions vary in their formulations, but all of them eject material from galaxies based on the local star formation rate and they have all been shown capable of regulating the growth of low mass galaxies in large scale simulations (e.g., Davé et al. 2011b; Kannan et al. 2013; Ocvirk et al. 2008).

Feedback from active galactic nuclei (AGN) is the result of energy and/or momentum injection that occurs as gas accretes onto the galaxy’s central super-massive black hole (BH). This is thought to be responsible for the rapidly-moving outflows that can be inferred from UV and X-ray observations of galaxies that host AGN (Chartas et al. 2002; Pounds et al. 2003; Reeves et al. 2003). It has been shown that AGN feedback is critical for heating gas in deep gravitational potentials (e.g., Sijacki & Springel 2006), shutting down star formation (e.g., Springel et al. 2005b,a; Croton et al. 2006; Hopkins et al. 2006; Sijacki et al. 2007; Hopkins et al. 2008a; Booth & Schaye 2009; McCarthy et al. 2010), and setting up self-regulated black hole growth (Di Matteo et al. 2005; Hopkins et al. 2006, 2007a,b, 2008b; Di Matteo et al. 2008; Younger et al. 2008; Sijacki et al. 2009).

Over the last few years, there have been many studies of galaxy formation using large-scale hydrodynamical simulations. For example, Schaye et al. (2010) presented a suite of smoothed particle hydrodynamics (SPH) simulations (the “OWLS” project) to explore the impact of various physical effects, like stellar and AGN feedback, on the resulting galaxy population. The simulations were used to examine, among other things, the evolution of the cosmic star formation rate (Schaye et al. 2010), observational signatures of the warm-hot intergalactic medium (Tepper-García et al. 2011, 2012), and the rates and modes of gas accretion into dark matter haloes (van de Voort et al. 2011; van de Voort & Schaye 2012; van de Voort et al. 2012). More recently, Davé

et al. (2011b) used SPH simulations to investigate the impact and importance of stellar winds. They found that stellar winds are able to reproduce the faint-end of the  $z = 0$  galaxy stellar mass function, while also leading to appropriate levels of enrichment in the inter galactic medium (Oppenheimer & Davé 2008; Oppenheimer et al. 2009). Even more recently, it was shown (Kannan et al. 2013) that large-scale hydrodynamical simulations are capable of producing galaxy stellar mass functions and stellar mass to halo mass relations that are consistent with observations by enforcing strong (Stinson et al. 2006) and early (Stinson et al. 2013) stellar feedback.

In the “GIMIC” project (Crain et al. 2009), roughly spherical volumes of size  $L \sim 20h^{-1}$  Mpc drawn from regions of various over-densities in the Millennium simulation were re-simulated at high resolution. This work has been used to study systematic variations in galaxy formation that scales with large scale environment (Crain et al. 2009), the formation (Font et al. 2011) and structure (McCarthy et al. 2012a) of galactic stellar haloes, and the characteristics (McCarthy et al. 2012b) and origin (Sales et al. 2012) of disk galaxies. The “Mare-Nostrum Horizon” (Ocvirk et al. 2008) is perhaps the largest, high-resolution, full-volume cosmological simulation run and it was performed using the Adaptive Mesh Refinement (AMR) simulation code RAMSES (Teyssier 2002). This simulation was used to study the mode of gas accretion into galaxies (Ocvirk et al. 2008) and the angular momentum evolution of high redshift galaxies (Danovich et al. 2012). Other simulations aimed at studying galaxy formation in large volumes have been carried out using RAMSES by Hahn et al. (2010) and Few et al. (2012).

Recently, a moving-mesh hydro solver was developed and incorporated into the hydrodynamical simulation code AREPO (Springel 2010). This method combines advantages of traditional Lagrangian hydro solvers (e.g., continuous resolution enhancement, adaptive geometry, Galilean invariance) with the strengths of Eulerian hydro solvers (e.g., instability handling, shock capturing, phase boundary resolution). It has been demonstrated that the hydro solver used in AREPO can lead to systematic changes in the properties of galaxies formed in cosmological simulations. In particular, the hot-haloes of galaxies are found to contain less hot gas (Vogelsberger et al. 2012) because it is able to cool efficiently onto the central gas disk (Sijacki et al. 2012; Kereš et al. 2012). This leads to an increase in hot-mode gas accretion rates (Nelson et al. 2013) and the creation of large, gas disks (Torrey et al. 2012). However, the first cosmological simulations published with this code lacked strong feedback, and therefore formed stars far too efficiently compared to actual galaxies.

The goal of this paper is to test and demonstrate the ability of the AREPO code to produce realistic galaxy populations directly in cosmological simulations by including realistic feedback processes. This paper builds on the work presented in Vogelsberger et al. (2013, hereafter, Paper I) where a detailed description of our galaxy formation model for the moving mesh code AREPO was presented for the first time. In Paper I, the framework of our approach was described in detail and a set of cosmological simulations were presented. The strength of the star formation driven winds and the AGN feedback parameters were tuned as to accurately reproduce the evolving cosmic star formation rate density and the redshift  $z = 0$  galaxy stellar mass function. The metal

content of ejected wind material was set to ensure a reasonable normalization of the redshift  $z = 0$  mass-metallicity relation. These relations, as well as several other redshift  $z = 0$  relations that were not used to tune the feedback model (e.g., the Tully-Fisher relation and luminosity functions) were presented in Paper I. The primary goal in what follows is to extend the analysis of Paper I by benchmarking the performance of our galaxy formation models against observational constraints at intermediate and high redshifts. This allows us to understand if the simulated galaxy populations are forming and evolving in a manner consistent with observations.

The structure of this paper is as follows: In Section 2 we describe the simulations that we have used, including a brief description of our general methods and the various feedback mechanisms included in our simulations. We present results of the build-up of stellar mass in Section 3, the evolution of the galactic and global star formation rates in Section 4, and the evolution of the mass-metallicity relation and Tully-Fisher relation in Section 5. We discuss our results and conclude in Section 6.

## 2 METHODS

The simulation suite used in this paper as well as a detailed description of our numerical methods have been discussed extensively in Paper I. We review briefly the main components of the galaxy formation model here.

All simulations used in this paper, apart from the ‘no-feedback’ run, include the same physics: gravity, hydrodynamics, radiative gas cooling, star formation with associated feedback, and AGN feedback. The gravity and hydrodynamics implementation are described in Springel (2010) and Vogelsberger et al. (2012). Radiative gas cooling for hydrogen and helium is carried out according to Katz et al. (1996) taking into account the presence of a cosmologically evolving ultraviolet background (Faucher-Giguère et al. 2009), which has been calibrated to match the mean transmission of the Lyman-alpha forest at redshifts  $z = 2-4.2$  (Faucher-Giguère et al. 2008b,a), HeII reionisation by  $z \sim 3$  (McQuinn et al. 2009), and complete HI reionisation by  $z = 6$ . In addition, the metal line contribution to the cooling rate is tabulated as a function of gas density, temperature, redshift-dependent background radiation, and metallicity using the photoionisation code CLOUDY (Ferland et al. 1998, 2013) and added to the primordial cooling rate. We correct both cooling contributions for self-shielding (Rahmati et al. 2013).

Star formation is modelled using a slightly modified version of the Springel & Hernquist (2003a) subgrid model which pressurises gas above the specified star formation density threshold and converts gas into stars according to a density based prescription that is tuned to recover the observed Kennicutt-Schmitt (Kennicutt 1998; Schmidt 1959) relation for star forming gas. The equation of state parameter used is  $q_{\text{eos}} = 0.3$ , which allows for resolution of internal disk structures yet prevents artificial gas fragmentation (Springel et al. 2005b; Robertson et al. 2006) and is also consistent with a value derived in the high-resolution ISM simulations of Hopkins et al. (2012b).

Stellar mass loss and metal enrichment are carried out by calculating the mass and composition of ejected material

from aging stellar populations at each time-step. To achieve this, we adopt a Chabrier (2003) initial mass function (IMF), the stellar lifetime function from Portinari et al. (1998), and the chemical yields for asymptotic giant branch (AGB) stars (Karakas 2010), core collapse supernovae (Portinari et al. 1998), and Type Ia supernovae (Thielemann et al. 1986). The star formation driven wind model uses a stochastic approach, similar to Springel & Hernquist (2003a), to launch wind particles out of star forming regions. We adopt a variable wind speed that drives winds at a velocity based on the local dark matter velocity dispersion (e.g., Oppenheimer & Davé 2006, 2008). The mass loading factor is adjusted appropriately based on the local velocity dispersion such that an equal amount of energy is transferred to the ISM per unit star formation rate (SFR) (Okamoto et al. 2010). We have introduced a wind metal loading factor,  $\gamma_w$ , which is set independently from the wind mass loading factor,  $\eta_w$ . The wind metal loading factor defines the relationship between the metallicity of newly created wind particles,  $Z_w$ , and the metallicity of the ambient ISM,  $Z_{\text{ISM}}$ , such that  $Z_{\text{wind}} = \gamma Z_{\text{ISM}}$ . We adopt a metal loading factor of  $\gamma_w = 0.4$  which allows for reasonable matches to the local and high redshift mass-metallicity relation, halo gas enrichment, and galaxy gas-phase metallicity gradients.

We adopt a unified model for quasar (Springel et al. 2005b; Di Matteo et al. 2005, 2008), radio (Sijacki et al. 2007), and radiative AGN feedback. The quasar mode self-regulates the black hole growth by injecting thermal energy around the black hole at a rate proportional to the black hole accretion rate. For lower accretion rates (in Eddington units), off-center radio-mode bubbles are generated. The AGN radiative feedback prescription provides a novel way for black holes to impact the gas state at large distances by suppressing gas cooling. While the majority of the gas in our cosmological box cools under the assumption of being exposed to a uniform UV background, the cooling rate of gas near BHs is calculated from a combination of both the uniform UV background and the ionising radiation field of nearby AGN.

All of the simulations in this paper were performed in periodic boxes of size  $L = 25 h^{-1} \text{Mpc}$ . The number of dark matter elements remains constant throughout the simulation with a particle mass dependent on the simulation resolution as noted in Table 1. The mass within individual resolution elements for the gas changes as material is advected across cell boundaries and the number of gas elements changes as cells can be converted into collisionless stellar particles and accreted by black holes. However, we include a cell (de-)refinement scheme (Vogelsberger et al. 2012) which enforces that all cells remain within a factor of two of a specified target mass so that the total number of baryonic elements in our simulations (star particles and gas cells) remains close to its initial value. All simulations use initial conditions generated at redshift  $z = 127$  based on a CAMB linear power spectrum. The adopted cosmological parameters are  $\Omega_{m0} = 0.27$ ,  $\Omega_{\Lambda0} = 0.73$ ,  $\Omega_{b0} = 0.0456$ ,  $\sigma_8 = 0.81$ , and  $H_0 = 100 h \text{ km s}^{-1} \text{ Mpc}^{-1} = 70.4 \text{ km s}^{-1} \text{ Mpc}^{-1}$  ( $h = 0.704$ ), which are consistent with Komatsu et al. (2011).

We study two types of simulations in this paper, both of which were described in Paper I. The first is a set of cosmological simulations of size  $L = 25 h^{-1} \text{Mpc}$  that initially contain  $256^3$  DM particles and  $256^3$  gas cells, and in which

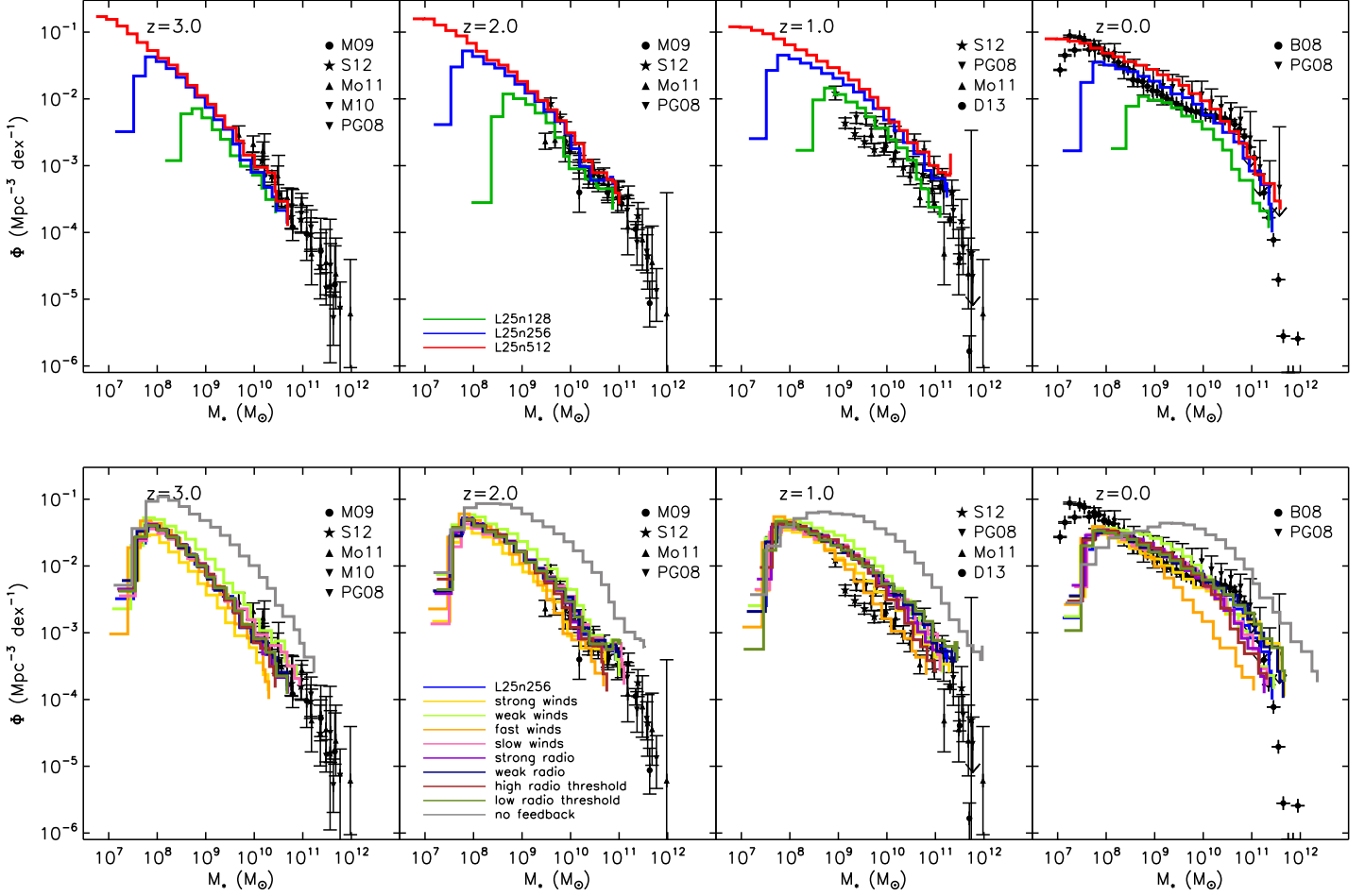


**Figure 1.** The simulated galaxy stellar mass function (GSMF) is shown for three different resolution simulations (top panel, solid coloured lines) and several variations of our feedback model (bottom panel, solid coloured lines) along with data points from observations at four different redshifts (as indicated). The “no feedback” simulation (grey line, bottom plot) provides a poor match to observations, underscoring the need for strong feedback to regulate the growth of galaxies. Many of the feedback models are able to alleviate the overproduction of stellar mass, including the high resolution fiducial model (red line, top plot) which provides reasonable agreement in the overall shape and normalisation of the GSMF compared against observations. This includes a flattening of the low mass end of the GSMF that occurs towards late times, along with a sharp cutoff for massive systems.

we vary the parameter choices for our feedback model. The impact of these feedback parameter variations on the redshift  $z = 0$  galaxy population was discussed in Paper I, and we extend this discussion here by comparing the simulated galaxy populations with high redshift data. The second set of simulations employs our fiducial feedback model at three different resolutions, and are labelled L25n128, L25n256, and L25n512. All our simulations are summarised in Table 1.

We use the SUBFIND algorithm (Springel et al. 2001) to identify gravitationally bound groups of dark matter, stars, and gas. We treat each self-bound group as a galaxy, and calculate its properties based on the SUBFIND (sub) halo catalogue. For the stellar mass, we could in principle take a sum over all stellar particles associated with the group. However, a non-negligible fraction of stellar mass in massive systems resides in a diffusely distributed component, as seen in observations of groups and clusters (e.g., Zibetti et al. 2005; McGee & Balogh 2010) and simulations (e.g., Murante et al. 2004, 2007; Rudick et al. 2006; Puchwein

et al. 2010; Puchwein & Springel 2013). This is an important point because: (i) intra-cluster light is not traditionally counted as contributing to the central galaxy’s mass and (ii) some of the intra-cluster light may fall below observational limits. To take this into account, we define the galactic stellar mass as the sum of stellar mass within twice the (total) stellar half mass radius. This has only a small effect on the stellar mass measurements for low mass systems, but can reduce the intra-cluster mass contributions in more massive systems. We have checked that our adopted definition of galactic stellar mass gives a similar result compared to what would be obtained if we used an observationally motivated surface brightness cut for massive systems (e.g., Rudick et al. 2006). For the halo mass we adopt the  $M_{200,\text{crit}}$  value, which is defined as the sum of all mass within a sphere where the halo’s average density is 200 times the critical density.

name	volume [ $(h^{-1} \text{ Mpc})^3$ ]	cells/particles	$\epsilon$ [ $h^{-1} \text{ kpc}$ ]	$m_{\text{DM}}/m_{\text{target}}$ [ $h^{-1} \text{ M}_{\odot}$ ]	physics
L25n512	$25^3$	$2 \times 512^3$	0.5/1.0	$7.33 \times 10^6 / 1.56 \times 10^6$	fiducial
L25n256	$25^3$	$2 \times 256^3$	1.0/2.0	$5.86 \times 10^7 / 1.25 \times 10^7$	fiducial
L25n128	$25^3$	$2 \times 128^3$	2.0/4.0	$4.69 \times 10^8 / 1.00 \times 10^8$	fiducial
stronger winds	$25^3$	$2 \times 256^3$	1.0/2.0	$5.86 \times 10^7 / 1.25 \times 10^7$	$\text{egy}_{\text{w}}/\text{egy}_{\text{w}}^0 = 6.0$
weaker winds	$25^3$	$2 \times 256^3$	1.0/2.0	$5.86 \times 10^7 / 1.25 \times 10^7$	$\text{egy}_{\text{w}}/\text{egy}_{\text{w}}^0 = 1.5$
faster winds	$25^3$	$2 \times 256^3$	1.0/2.0	$5.86 \times 10^7 / 1.25 \times 10^7$	$\kappa_{\text{w}} = 7.4$
slower winds	$25^3$	$2 \times 256^3$	1.0/2.0	$5.86 \times 10^7 / 1.25 \times 10^7$	$\kappa_{\text{w}} = 1.85$
stronger radio	$25^3$	$2 \times 256^3$	1.0/2.0	$5.86 \times 10^7 / 1.25 \times 10^7$	$\epsilon_{\text{m}} = 0.7$
weaker radio	$25^3$	$2 \times 256^3$	1.0/2.0	$5.86 \times 10^7 / 1.25 \times 10^7$	$\epsilon_{\text{m}} = 0.175$
higher radio threshold	$25^3$	$2 \times 256^3$	1.0/2.0	$5.86 \times 10^7 / 1.25 \times 10^7$	$\chi_{\text{radio}} = 0.1$
lower radio threshold	$25^3$	$2 \times 256^3$	1.0/2.0	$5.86 \times 10^7 / 1.25 \times 10^7$	$\chi_{\text{radio}} = 0.025$
no AGN	$25^3$	$2 \times 256^3$	1.0/2.0	$5.86 \times 10^7 / 1.25 \times 10^7$	stellar winds; no AGN feedback
no feedback	$25^3$	$2 \times 256^3$	1.0/2.0	$5.86 \times 10^7 / 1.25 \times 10^7$	no stellar/AGN feedback

**Table 1.** Summary of the different cosmological simulations as originally described in Paper I, and as referenced throughout this paper. The L25n128, L25n256, L25n512 simulations employ the fiducial physics parameters shown in Table 1 of Paper I. The remaining simulations explore variations in our feedback model parameters at the intermediate resolution. Parameters that are varied are indicated in the last column.

### 3 THE STELLAR CONTENT OF GALAXIES

The shape of the galaxy stellar mass function (GSMF) is determined by a combination of the underlying DM (sub)halo mass function (HMF), and the efficiency with which stars are formed in those haloes. As noted previously, including winds driven by star formation is critical to reproducing the evolving number density of low mass galaxies (Oppenheimer et al. 2010; Bower et al. 2012; Puchwein & Springel 2013) while AGN feedback can quench star formation in massive haloes, establishing a high mass cutoff in the GSMF (Croton et al. 2006; Hopkins et al. 2008a; Gabor et al. 2011; Bower et al. 2012; Puchwein & Springel 2013). Both of these feedback processes have been included in our simulations as described in the previous section, and as has already been shown in Paper I the model included in our simulations is capable of producing reasonable matches to the GSMF at redshift  $z = 0$ . In this section, we focus on the evolution of the GSMF with time, and compare the simulation results with several recent observations (summarised in Table 2). We have applied appropriate correction factors to all observational stellar mass measurements so that all results are now appropriate for a Chabrier (2003) initial mass function (IMF).

A comparison of the simulated GSMF with observations is presented in Figure 1. The bottom panel of Figure 1 shows the simulated GSMF for several variations of our feedback model. Most of the feedback models provide satisfactory fits to the redshift  $z = 3$  GSMF. The one exception is the “strong winds” simulation, which suppresses the stellar mass growth of galaxies slightly too efficiently, and lowers the normalisation of the simulated GSMF. By redshift  $z = 2$  the offset of the strong wind model is less distinct, and all of the feedback runs provide good fits to the observational data, especially compared to the “no feedback” case. At redshift  $z = 1$  most of the feedback models deviate from observations in the normalisation of the GSMF at the low mass end. This is an indication that low mass systems in our sim-

ulations are building up their stellar mass at this epoch more efficiently than observations indicate. The exception is the “fast wind” model, which produces a GSMF that is offset toward lower normalisations (compared to the other feedback models), consistent with observations. By redshift  $z = 0$ , this normalisation offset is reduced for most of the feedback models, as the observed number density of low mass systems has substantially increased, while the number density of these same objects has remained fairly constant in the simulations. While the “fast wind” simulation provided the best fit to the GSMF at redshift  $z = 1$ , this same simulation now strongly underproduces galaxies just below the knee of the GSMF.

Our simulation shows an appropriate exponential cutoff in the GSMF at low redshift for massive galaxies. The simulation box used here is too small to identify this exponential cutoff clearly at early redshifts. Where it is seen, the exponential drop is driven by efficient AGN radio-mode feedback in our simulations which suppresses star formation in massive systems (Croton et al. 2006; Hopkins et al. 2008a; Guo et al. 2010; Bower et al. 2012; Puchwein & Springel 2013). The exact location of this cutoff depends on choices for the AGN radio feedback strength and accretion threshold, as discussed in Paper I. Obtaining this cutoff is important because it indicates that all haloes will have reasonably sized stellar components associated with them. This allows for a clear connection between the properties (i.e. the growth rates, concentrations, morphologies, etc.) of observable galaxies and their host dark matter haloes.

The resolution dependence of the simulated GSMF is shown for the fiducial feedback model in the top panel of Figure 1. We note three points regarding the numerical convergence of the simulated GSMF. First, any resolution effects become increasingly prominent toward late times. Although all three resolution simulations agree fairly well at redshift  $z = 3$ , the redshift  $z = 0$  agreement is less good. Second, while there is an offset between the normalisations of the lowest resolution ( $128^3$ ) simulation and the higher

**Table 2.** Observational references for the galaxy stellar mass function data used in Figure 1.

Source	Observed Redshift Range	Plotted Redshift Panel	Original IMF
Baldry et al. (2008)	$z < 0.05$	$z = 0$	diet Salpeter
Pérez-González et al. (2008)	$0.0 < z < 0.2$	$z = 0$	Salpeter
	$1.0 < z < 1.3$	$z = 1$	Salpeter
	$2.0 < z < 2.5$	$z = 2$	Salpeter
	$3.0 < z < 2.5$	$z = 3$	Salpeter
Marchesini et al. (2009)	$2.0 < z < 3.0$	$z = 2$	Kroupa
	$3.0 < z < 4.0$	$z = 3$	Kroupa
Marchesini et al. (2010)	$3.0 < z < 4.0$	$z = 3$	Kroupa
Mortlock et al. (2011)	$1.0 < z < 1.5$	$z = 1$	Salpeter
	$2.0 < z < 2.5$	$z = 2$	Salpeter
	$3.0 < z < 3.5$	$z = 3$	Salpeter
Santini et al. (2012)	$1.0 < z < 1.4$	$z = 1$	Salpeter
	$1.8 < z < 2.5$	$z = 2$	Salpeter
	$2.5 < z < 3.5$	$z = 3$	Salpeter
Davidzon et al. (2013)	$0.9 < z < 1.1$	$z = 1$	Chabrier

resolution simulation GSMFs which is visible at late times, the offset between the intermediate ( $256^3$ ) and high ( $512^3$ ) resolution simulations GSMFs is smaller. This indicates that our results are converging numerically. Third, the GSMF for high mass systems (e.g.,  $M_* > 10^{10} M_\odot$ ) shows little offset at any redshift for the two highest resolution simulations, which indicates these systems are numerically converged. In fact, it is likely that the GSMF is converged down to even lower masses (e.g.,  $M_* > 10^9 M_\odot$ ) for our highest resolution simulations. However, we could only demonstrate this point by presenting an even higher resolution simulation, which is beyond the scope of this paper.

A clear characterisation of the performance of our various feedback models can be obtained by independently assessing the evolution of the slope and normalisation of the low mass end of the GSMF. As mentioned above, the majority of our feedback models appear to overproduce the number density of low mass galaxies at redshift  $z = 1$ . The right panel of Figure 2 highlights this by showing the number density evolution of simulated low mass galaxies (in the same particular mass bin used in Weinmann et al. 2012). Weinmann et al. (2012) argued that the shape of the low mass galaxy number density evolution in previous semi-analytic and hydrodynamical modeling is characteristically distinct from that of the observations, indicating that the models were not using wind prescriptions capable of decoupling the galaxy stellar mass growth from the underlying halo mass growth. Here, we find that all of our feedback choices lead to a very flat evolution in the number density of these low mass systems past redshift  $z = 1$ . Variations in our adopted wind model set the normalisation of the low redshift number density plateau, but do not strongly impact the slope. Whereas the “weak winds” model leads to a higher number density of

low mass systems, the “strong winds” model decreases the number density of low mass systems. Since all of our models plateau in their low mass number density at late times while the observations indicate an increasing number density of these systems, it is unlikely that any simple variation in our wind model could reproduce the observed redshift  $z = 1$  and  $z = 0$  low mass galaxy number densities simultaneously. It is worth noting here that, as expected, variations in the adopted black hole feedback model parameters have negligible impact on the evolution of the simulated low mass galaxy population.

The left panel of Figure 2 demonstrates the resolution dependence of the number density evolution of low mass galaxies. All resolution simulations show the same characteristic evolutionary shape. Higher resolution simulations produce slightly higher normalisations, due to increases in the star formation efficiency in low mass galaxies. The magnitude of this resolution dependence decreases towards better resolved systems. The highest resolution model passes above most of the low redshift data points and misses the intermediate redshift data points. This may be an indication that our models require more efficient suppression of star formation in low mass systems at these redshifts. But, as discussed above, while simply tuning up the strength of our wind feedback model could correct the normalisation of the low mass galaxy number density at either low or intermediate redshifts, we cannot correct the normalisation at both epochs simultaneously.

The slope of the low mass end of the GSMF is observed to flatten towards low redshifts. The slope of the low mass end of the simulated GSMF mimics this observed flattening. Fitting a Schechter (1976) function to the simulated GSMF explicitly demonstrates this evolution. The right panel of

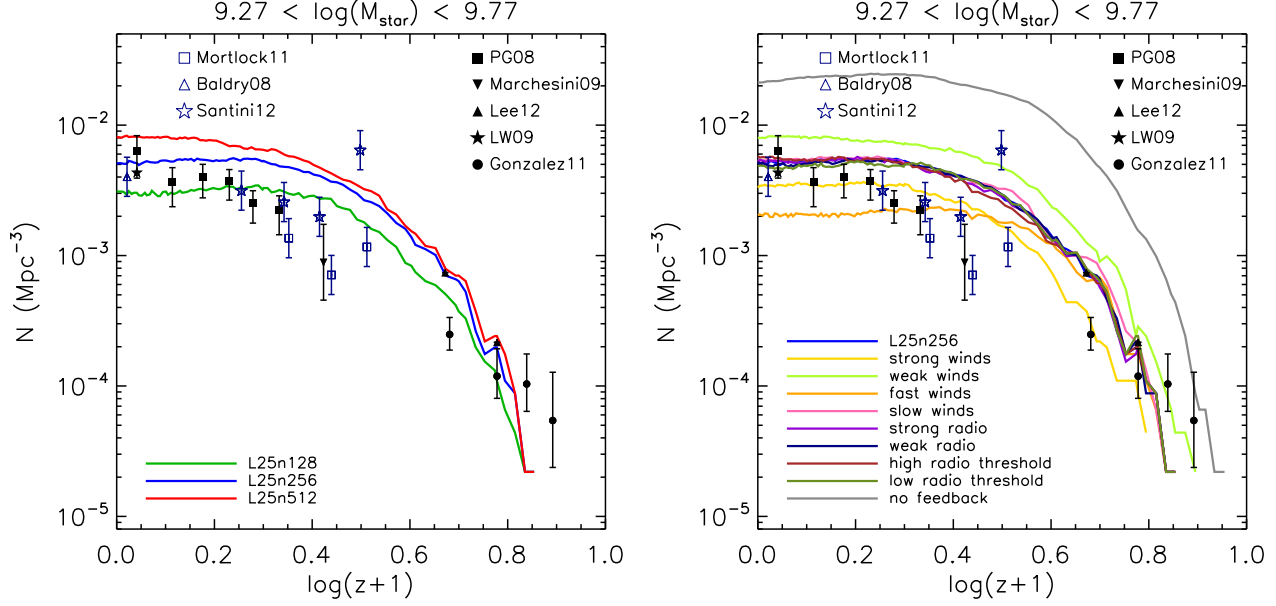


**Figure 2.** The evolution of the number density of low mass galaxies is shown for three different resolutions (left) and our varied feedback models (right). The black symbols show the data taken directly from the Weinmann et al. (2012) paper, while the blue points show additional data points assembled by interpolating/extrapolating the GFMS data used in Figure 1 of this paper. As in many semi-analytic and hydrodynamic models, low mass systems are being assembled too early, leading to an overproduction of these systems by redshift  $z \sim 1$ , with little evolution in their number density thereafter. Variations in the feedback parameters lead to adjusted normalisations for the late time number density plateau, without substantially impacting the late time slope.

Figure 3 shows the low mass end slope,  $\alpha$ , compared to observational results for the various feedback model parameterisations. Here we note that Pérez-González et al. (2008) caution that their estimations of the low-mass end slope of the GSMF above redshift  $z \gtrsim 2$  could be affected by incompleteness. Thus, as indicated in the legend of Figure 3, we have removed the  $z > 2$  slope calculations of Pérez-González et al. (2008). Most of the simulations are clustered around a single evolutionary track that traces the observed low mass end slope evolution. We do not show a best fit  $\alpha$  value for the “no feedback” simulation because the low redshift GSMF is not well described by a single Schechter function. The most substantially offset model is the “fast wind” model, which has a steeper slope than observations (see Figure 1 and discussion above). All of the other feedback models produce evolving low mass end slopes which are similar to the observations.

There is no major resolution dependence to this result, as demonstrated in the left panel of Figure 3. The fiducial feedback model yields very similar low mass end GSMF slopes for all three resolutions. In particular, the intermediate and high resolution runs show very similar low redshift behaviour, indicative of numerical convergence.

### 3.1 Luminosity Function

Comparing our simulated GSMFs to observations implicitly assumes that the observed spectra can be converted into stellar mass measurements accurately. Stellar mass measurements are typically obtained from observations by employing stellar population synthesis models (e.g., Leitherer et al. 1999; Bruzual & Charlot 2003; Le Borgne et al. 2004) and

assuming some star formation history and IMF. However, there are a number of uncertainties associated with observationally determined stellar mass measurements, and so some caution should be taken when comparing to theoretically determined stellar mass measurements (Mitchell et al. 2013). Instead of considering the stellar mass function comparison of the previous subsection alone, it is useful to also consider how the luminosity functions compare between the simulations and observations. To facilitate this comparison, we assign broad band luminosities to all star particles in each galaxy via the Bruzual & Charlot (2003, hereafter BC03) catalogues after taking into account the star particle’s age, initial stellar mass, metallicity, and assuming a Chabrier (2003) IMF. To start, we neglect the impact of dust attenuation, and tabulate each galaxy’s luminosity as the sum of the contributions from all of its star particles.

It was shown in Paper I that our galaxy formation model produces luminosity functions that agree with local SDSS  $g$ -,  $r$ -,  $i$ -, and  $z$ -band measurements. To extend the comparison of the observed and simulated results to higher redshift, we consider the rest-frame B-band luminosity function versus redshift as shown in Figure 4. Observational data points are included for comparison as outlined in Table 3. As in Figure 1, the top panel of Figure 4 shows the resolution dependence of the simulated redshift dependent luminosity function while the bottom panel shows the impact of the feedback model parameter choices on the simulated luminosity function.

The luminosity function is impacted by feedback in a very similar way to the GSMF. Most of the feedback models provide satisfactory fits to the redshift  $z = 3$  luminosity function, though the observational luminosity function

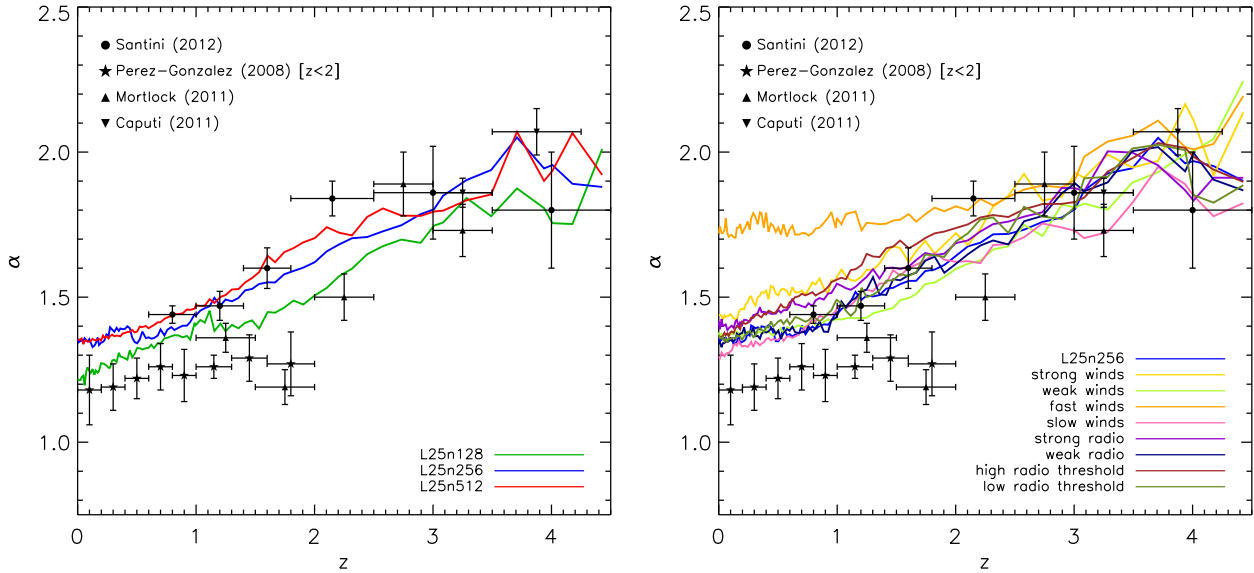


**Figure 3.** The evolution of the low mass end slope of the galaxy stellar mass function is shown for three different resolutions (left) and our varied feedback models (right). We have obtained the  $\alpha$  slope value by performing an RMS minimisation to determine the best fit Schechter function parameters. Observational estimates of  $\alpha$  from the literature are also shown.

is offset towards marginally brighter values. Since no substantial offset exists in the redshift  $z = 3$  GSMF simulation/observation comparison at the same number density, this may be an indication that our simulated systems need marginally higher star formation rates (i.e. have somewhat younger stellar populations) to better match the B-band luminosity function. This, however, may give rise to other tensions in either the global star formation rate density or star formation main sequence relations which we discuss in the next section. It is also possible that omitting non-stellar sources of luminosity (e.g., AGN) could be leading to an underestimation of simulated galaxies true B-band luminosities.

At redshifts  $z = 2$  and  $z = 1$  we find very good agreement between the simulated and observed luminosity functions in terms of overall shape and normalisation for most of the feedback models. The two clear outlier simulations are the “no feedback” case (which allows for efficient star formation in all galaxies, making haloes/galaxies of a given number density too bright) and the “fast wind” case (which suppresses star formation in massive systems too efficiently, and therefore underproduces bright objects). As with the GSMF, the various model parameter choices for the AGN feedback have little impact here, because of the lack of very massive/bright objects in our small simulation volume. By redshift  $z = 0$ , there is a broader spread in the luminosity functions that result from the different models, with the best agreement to the observed B-band luminosity function being given by our fiducial “L25n256” model, as discussed in Paper I.

The resolution dependence of the simulated luminosity function is demonstrated for our fiducial feedback model in the top panel of Figure 4. There is a slight increase in the normalisation of the luminosity function for higher resolution simulations, however this normalisation offset is small

between the intermediate and high resolution cases. Overall, the similarity of the intermediate and high resolution simulations indicates reasonable numerical convergence for our fiducial feedback model.

To this point, we have neglected the impact of dust attenuation which can have a substantial impact on the measured B-band luminosity function (e.g., Tuffs et al. 2004; Pierini et al. 2005). We can approximate the dust attenuation correction to the simulated B-band luminosity function using the simple model of Charlot & Fall (2000). The dust attenuated B-band luminosity functions from our models are shown in the top panel of Figure 4 as a series of colored dashed lines. The size of the correction is  $\sim 0.5$  magnitudes, and pushes our models away from the observations at all redshifts. This exacerbates the previously discussed shortfall of our models with respect to the bright end of the luminosity function at redshift  $z = 3$ , and creates a similar issue at lower redshifts. However, the normalization and slope of the faint end of the luminosity function remains almost unchanged where our models continue to provide a good match to the observations. More detailed modeling of the dust attenuation will be considered in future work via three-dimensional radiative transfer to self-consistently determine line-of-sight attenuation factors under more explicit assumptions (e.g., the dust-to-gas ratio) which may validate or correct the luminosity functions presented here.

In general, the simulated luminosity functions agree well with observations up to redshift  $z = 3$ . Perhaps this is somewhat expected, given that: (i) we have already shown reasonable agreement in the stellar mass function and (ii) we are converting stellar masses into broad band luminosities using similar techniques that observers use to convert broad band luminosities into stellar masses. Moreover, it has been shown previously in semi-analytic models that good matches can be achieved to the evolving B-band luminosity function by



**Table 3.** Observational references for the luminosity function data used in Figure 4.

Source	Observed Redshift Ranges	Plotted Redshift Panel
Poli et al. (2003)	$0.7 < z < 1.0$	$z = 1$
	$1.3 < z < 2.5$	$z = 2$
	$2.5 < z < 3.5$	$z = 3$
Gabasch et al. (2004)	$0.8 < z < 1.2$	$z = 1$
	$1.75 < z < 2.5$	$z = 2$
	$2.5 < z < 3.4$	$z = 3$
Giallongo et al. (2005)	$0.7 < z < 1.0$	$z = 1$
	$1.3 < z < 2.5$	$z = 2$
	$2.5 < z < 3.5$	$z = 3$
Ilbert et al. (2005)	$0.05 < z < 0.2$	$z = 0$
	$1.0 < z < 1.3$	$z = 1$
Faber et al. (2007)	$0.2 < z < 0.4$	$z = 0$
	$1.0 < z < 1.2$	$z = 1$
Marchesini et al. (2007)	$2.0 < z < 2.5$	$z = 2$
	$2.5 < z < 3.5$	$z = 3$

accounting for the finite recycling time for previously ejected wind material (Henriques et al. 2012) as is done in our simulations (see discussion in Oppenheimer & Davé 2008, for more details on the recycling time for wind material). The two most obvious ways that we could have achieved agreement in the stellar mass functions without obtaining similar agreement in the luminosity functions is by forming galaxies in our simulation with very different star formation histories from that assumed by observational models, or, if our assumption of neglecting dust attenuation failed severely. It is unlikely that we have formed galaxy populations with very different formation histories because, as we will show in the next section, the simulated global SFR as well as the simulated star formation main sequence both follow observations reasonably well. While we have not carried out a full radiative transfer calculation to determine the impact of dust attenuation, we have shown that our fiducial models only slightly undershoot the observational measurements of the B-band luminosity function when we approximate dust attenuation via the simple model of Charlot & Fall (2000).

### 3.2 Stellar Mass vs. Halo Mass

Within the past decade, abundance matching models have brought together measurements of the galaxy stellar mass functions with detailed numerical models of structure formation (Conroy et al. 2006; Conroy & Wechsler 2009; Moster et al. 2010; Guo et al. 2010; Moster et al. 2012; Behroozi et al. 2012). By relying on a simple central assumption to pair the population of simulated dark matter haloes to observed galaxies (e.g., based on mass), a more detailed link between observed galaxies and their host dark matter haloes has been established along with an understanding of how

galaxies and their host haloes evolve together in time. In particular, one of the central results from these models is a parameterised relationship describing the evolution of the stellar mass to halo mass (SMHM) ratio as a function of galaxy mass and redshift. Comparing directly to abundance matching results – rather than using just the GSMF comparison in the previous section – has the added advantage that abundance matching models account for the asymmetric impact of observational errors on the stellar mass functions, while also inferring additional galaxy properties such as their star formation rates.

It has been shown in Paper I that the feedback physics included in our simulations produces a reasonable match to the abundance matching derived SMHM relationship at redshift  $z = 0$  by reducing the efficiency of star formation in low mass and high mass haloes through efficient stellar and AGN feedback. Here, we focus on the evolution of the SMHM ratios for the simulated galaxies compared against the abundance matching models of Moster et al. (2012) and Behroozi et al. (2012) at several redshifts, as well as Guo et al. (2010) at redshift  $z = 0$ . Figure 5 shows the simulated galaxy stellar mass vs. halo mass relation for three different redshifts. The solid lines indicate the median SMHM relation as a function of simulation resolution (top panel) and feedback model (bottom panel). In each figure, we show a two-dimensional histogram indicating the full distribution of simulated galaxies for the “L25n256” simulation (bottom panel) and “L25n512” simulation (top panel).

In the low mass regime at redshift  $z = 0$ , most of the feedback models yield SMHM relations clustered around the abundance matching results. The spread in these models can be attributed to changes in the adopted wind model, as discussed in Paper I. Briefly, we note that the “strong” wind model suppresses star formation in low mass systems too efficiently, leading to an underestimate of the SMHM relation. Conversely, the “weak” wind simulation overproduces stars in these same systems. As we consider these relations at higher redshift, a similar trend remains true. At redshifts  $z = 1$  and  $z = 2$  the “weak” wind and “strong” wind models bracket the abundance matching SMHM relation, with approximately the correct slope. The fiducial feedback model, which falls between these two cases, is in approximate agreement with the abundance matching results (although the slope may be somewhat steeper at redshift  $z = 2$  in Behroozi et al. 2012).

For high mass systems at redshifts  $z = 1$  and  $z = 0$ , the relationship between the abundance matching SMHM relation and the simulation result is heavily dependent on the adopted AGN feedback model. As discussed in Paper I, the location of the knee of the SMHM relation is set by the adopted AGN radio threshold; i.e. a high radio threshold pushes the knee location to lower masses. The adopted radio threshold value was set to get the redshift  $z = 0$  SMHM relation knee in the right location. The same trend can be observed at redshift  $z = 1$ . Notably, the high and low radio threshold values bracket the desired location of the SMHM relation knee.

The top panel of Figure 5 shows the resolution dependence of the simulated SMHM relation using our fiducial feedback model. While the redshift  $z = 2$  SMHM relation is converged for the intermediate and high resolution simulation, the lowest mass systems show an offset between these

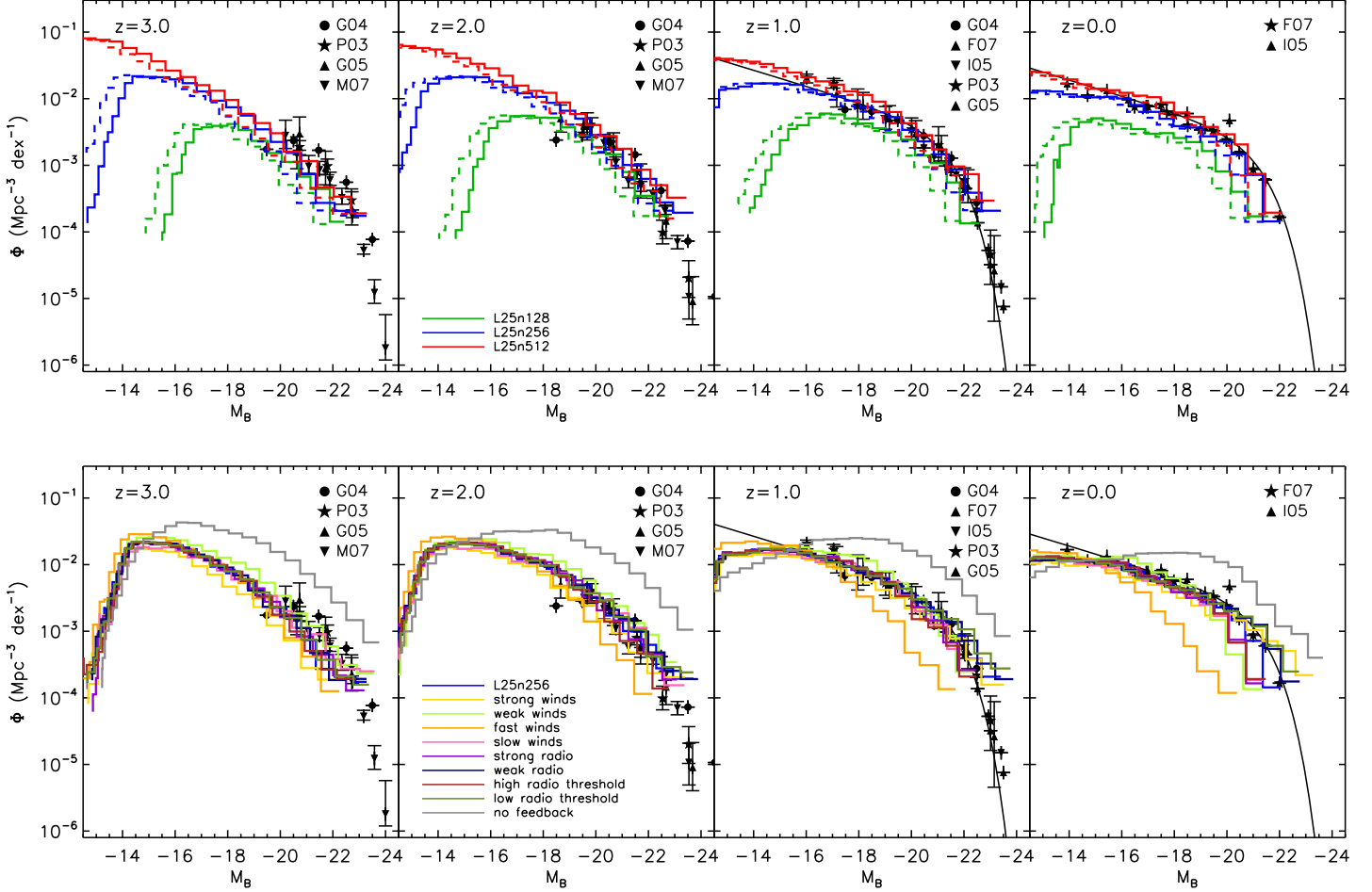


**Figure 4.** B-band luminosity functions compared against observational data at several redshifts for three different resolutions (top) and our varied feedback models (bottom). The solid lines assume no dust attenuation. The dashed lines (top panel only) show the attenuated luminosity function using the simple model of Charlot & Fall (2000). The varied physics models impact the simulated luminosity function similarly to the GSMF. The agreement between our simulations and observations is good for redshifts  $0 \leq z \leq 2$ , while the redshift  $z = 3$  comparison shows a slight offset between the observations and simulations. As with the stellar mass function, we find an evolution toward somewhat steeper low luminosity slopes at high redshift for the simulation data.

two runs at redshift  $z = 1$  which becomes more pronounced by redshift  $z = 0$ . There is a factor of  $\sim 2$  offset in the stellar masses of the intermediate and high resolution runs for low mass systems at redshift  $z = 0$ . While the intermediate resolution simulation agrees well with the Behroozi et al. (2012) result, the high resolution simulation agrees better with the Moster et al. (2012) result. Although the “strong winds” simulation suppressed star formation too efficiently in low mass systems in the intermediate resolution simulation, it may provide a good fit to the SMHM relation at high resolution.

Interestingly, the high resolution simulation (red line) SMHM relation is in good agreement with the Moster et al. (2012) abundance matching relation at redshifts  $z = 0$  and  $z = 2$ , but is slightly offset from the Moster et al. (2012) relation at redshift  $z = 1$ . At redshift  $z = 1$ , the simulated low mass galaxies have more stellar mass than we would expect from abundance matching models. The offset between the simulations and abundance matching results is roughly a factor of two in stellar mass. This is directly related to the

flat evolution of the number density of low mass systems demonstrated in Figure 2, and is another indication that the simulated low mass galaxies are building up stellar mass too rapidly at or around redshift  $z = 1$ . As discussed previously, stronger star formation driven winds can suppress stellar masses buildup in these systems leading to better agreement at redshift  $z = 1$ . However, this comes at the expense of the agreement between the abundance matching and simulation redshift  $z = 0$  SMHM relationship. It is therefore interesting to consider whether alternative galactic wind implementations which have successfully reproduced the normalisation, slope, and scatter of the SMHM relation at intermediate and high redshift will achieve similar agreement at low redshifts (e.g., Kannan et al. 2013).

We conclude that our fiducial feedback model is capable of reproducing the abundance matching derived SMHM relation to within a factor of two in galaxy stellar mass at all plotted redshifts. This is an important result because it implies that we can compare simulated galaxies against observed galaxies by matching them based on their stellar

mass. This also implies that the galaxies in our simulations are building up their stellar mass similarly to what is inferred via abundance matching models (modulo the discussion of the low mass systems around redshift  $z = 1$ ). We note that Moster et al. (2012) highlighted the fact that while many simulations reproduce the redshift  $z = 0$  SMHM relation correctly, their intermediate and high redshift SMHM relations lie far from abundance matching results. Although our fiducial model slightly overproduces the stellar mass content of low mass galaxies at early times, we emphasize that the magnitude of this overproduction is an improvement over many previous results (Moster et al. 2012).

## 4 SFR RELATIONS

In the previous section we examined the simulated GSMF and SMHM relationships, finding that our feedback models are capable of producing galaxy populations that build up stellar mass consistent with observations. To further differentiate the performance of our various feedback model choices, we consider additional constraints on how and when galaxies build up their stellar mass from direct observations of the evolution of the global star formation rate and star formation main sequence. We contrast the results of our various feedback models with those observations in the following subsections.

### 4.1 Cosmic SFR Density

The global cosmic SFR density (SFRD) has been measured out to high redshift in several bands including the UV (Yoshida et al. 2006; Salim et al. 2007; Bouwens et al. 2009; van der Burg et al. 2010; Robotham & Driver 2011; Bouwens et al. 2011; Cucciati et al. 2012), radio (Smolčić et al. 2009; Karim et al. 2011), UV/IR (Zheng et al. 2007), and FIR (Rujopakarn et al. 2010). There is an increasingly clear picture for the cosmic SFRD emerging, where the SFRD increases substantially from redshift  $z \sim 10$  to  $z \sim 2$  (Madau et al. 1998; Bouwens et al. 2008), reaches a peak value around redshift  $z = 2 - 3$ , and then begins to decline rapidly thereafter (Lilly et al. 1996; Schiminovich et al. 2005; Hopkins & Beacom 2006; Villar et al. 2008). While the SFRD is generally limited by the growth rate of dark matter haloes at high redshift (e.g., Hernquist & Springel 2003), the location of the turnover of the SFRD function as well as the steepness of the subsequent decline depend heavily on the implementation of feedback physics (e.g., Springel & Hernquist 2003b; Schaye et al. 2010; Crain et al. 2009; Bower et al. 2012). The role of feedback in shaping the SFRD for the particular set of simulations used in this paper has been discussed in Paper I. Here, we extend the discussion of Paper I by identifying which haloes have had their star formation rates impacted the most by feedback and relating this to the build-up of stellar mass discussed in the previous section. We note that although the simulation box used here is relatively small, it has been previously shown that this box should be sufficiently large to capture the proper late time evolution of the cosmic SFRD (Springel & Hernquist 2003b).

Figure 6 shows the global cosmic SFRD as a function of redshift, broken down as a function of galaxy stellar mass.

The three panels show three distinct feedback models: “no feedback” (left), “no AGN” (center), and “L25n256” (right).

The “no feedback” simulated SFRD substantially overshoots the observed data points at all redshifts. At early times (i.e.  $z \gtrsim 3$ ) the largest contribution to the SFRD is from relatively “low mass” galaxies. These systems do not yet harbour sufficiently massive black holes to regulate their growth via AGN feedback. Instead, we find that including star formation driven winds is sufficient to regulate the early SFRD to an observationally consistent level, as demonstrated in the central panel of Figure 6. The impact of introducing winds can be seen very clearly by identifying the blue/green lines which trace the SFRD contributions from low mass systems. Galactic winds: (i) reduce the early peak SFRs in low mass systems and (ii) increase the SFR contributions from low mass systems at late times.

Correcting the late time behaviour of the SFRD evolution requires the introduction of AGN feedback to regulate the growth of massive systems (e.g., Schaye et al. 2010). Without strong AGN feedback, the SFRD continues to rise past redshift  $z = 2$  with dominant contributions from systems with  $M_* > 10^{10} M_\odot$  as seen in the central panel of Figure 6. In fact, Figure 6 shows that the contributions from the most massive systems *alone* are enough to exceed the observed global cosmic SFRD limits. When we introduce AGN feedback into our models, as shown in the right panel of Figure 6, star formation is suppressed in haloes with stellar masses  $M_* > 10^{10.5} M_\odot$  allowing our models to pass through the observational data points with the correct late time slope (e.g., Bower et al. 2012). Importantly, we note that the mass scale where AGN feedback must kick in to regulate the cosmic SFRD evolution at late times is the same mass scale where star formation must be suppressed in order to reproduce the observed location of the “knee” of the GSMF.

As was concluded in Paper I, we find good agreement of our fiducial feedback model’s simulated SFRD with the measured cosmic SFRD. The late time shape is mainly regulated by AGN feedback, whereas the early build-up of stellar mass is mainly limited through stellar feedback.

### 4.2 Star Formation Main Sequence

The star formation main sequence (SFMS) describes the relationship between galactic stellar mass and star formation rate (e.g., Noeske et al. 2007; Daddi et al. 2007; Elbaz et al. 2007; Salim et al. 2007; Peng et al. 2010; Whitaker et al. 2012). Not only is there a clear correlation between stellar mass and star formation rate, but the normalisation of this relationship evolves with redshift while the slope remains nearly constant (Daddi et al. 2007; Dutton et al. 2010). Moreover, as a result of the observed small scatter, it has been argued that galaxies spend the vast majority of their lives on or close to this relationship, and thus the SFMS is the primary avenue along which galaxies accumulate their stellar mass (Noeske et al. 2007). Comparing against the observed SFMS provides an additional constraint on the build-up of stellar mass in our simulations.

Figure 7 shows the SFMS for our various feedback models at redshifts  $z = 2$ ,  $z = 1$ , and  $z = 0$ . In each panel, we show a two-dimensional histogram denoting the distribution of galaxies from the “L25n256” simulation (bottom panels)

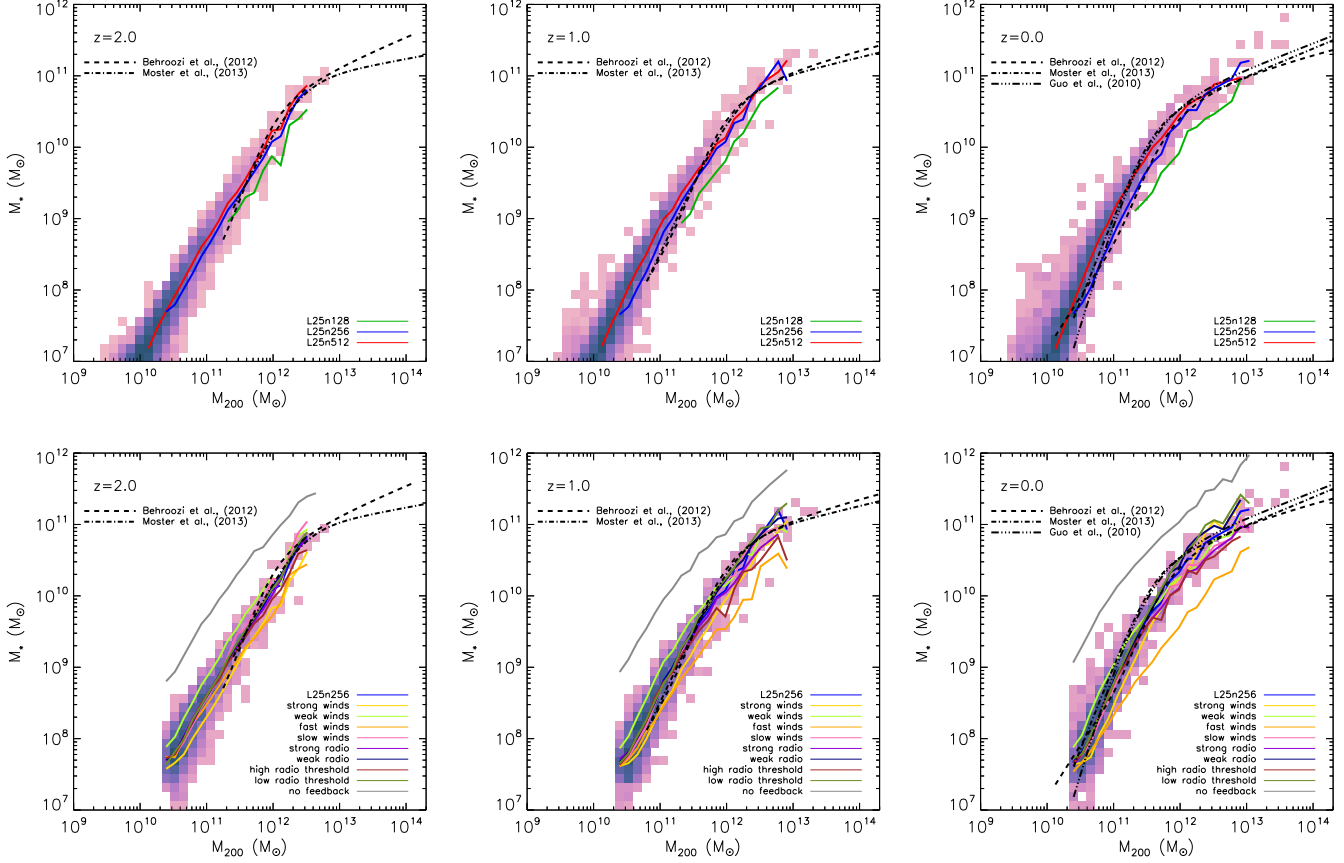


**Figure 5.** Binned median stellar-mass halo-mass relations are shown for three different resolutions (top) and our varied feedback models (bottom) as solid lines for redshifts  $z = 2$ ,  $z = 1$ , and  $z = 0$  from left to right, respectively. In the background, two dimensional histograms show the distribution of simulated galaxy’s stellar masses and halo masses, for the L25n512 (top) and L25n256 (bottom) simulations. Each panel also contains lines denoting the results of abundance matching studies, as labelled in the plotted regions.

and the “L25n512” simulation (top panels). Additionally, we show coloured lines marking the binned median SFMS for the various feedback models (bottom) and resolutions (top, as noted in the plotted legend). Observational SFMS measurements are shown within the figures for comparison against our models.

All feedback models recover a positive correlation between the galaxy stellar mass and star formation rate. To parametrise and quantify this relationship, we adopt a functional form for the SFMS of

$$\log \left( \frac{\text{SFR}}{\text{M}_{\odot} \text{yr}^{-1}} \right) = \log \left( \frac{\text{SFR}_{10}}{\text{M}_{\odot} \text{yr}^{-1}} \right) + b \log \left( \frac{M}{10^{10} \text{M}_{\odot}} \right) \quad (1)$$

where  $\text{SFR}_{10}$  and  $b$  set the normalisation and slope of the relation, respectively. A best fit is found via RMS minimisation of the simulated galaxies in a given simulation. The derived best fit for the “L25n256” simulation (bottom) and the “L25n512” simulation (top) is shown as a solid black line in Figure 7, with the best fit parameters printed within the plotted region. We fit Gaussian curves to this residual distribution, and present the one sigma standard deviation within the plotted region to indicate the intrinsic spread in the simulated relations. Although it is not explicitly shown for all cases, these relations tend to have a fairly tight scatter. The scatter about this relationship is  $\sigma_{\text{MS}} \sim 0.3$  dex

for both the “L25n256” and “L25n512” simulations, which is very similar to the observed scatter (Noeske et al. 2007; Salmi et al. 2012). Our fiducial feedback models naturally recover a SFMS with an intrinsic scatter that is similar to observations. Here, we consider how the normalisation and slope of the simulated SFMS compare to observations and the role that our feedback model plays in achieving this result.

Most of our feedback models fall slightly below the observed SFMS normalisations. This generalisation includes models with both strong/weak winds and strong/weak radio mode AGN. In particular, if we examine redshift  $z = 2$  results, we find that all of our models (except for the “fast wind” simulation, which is clearly the worst fit) produce very similar SFMS relations which are all about 0.3 dex below the observed relation and all have a slope of close to unity, which is steeper than the observed relation. In most of the previously discussed plots, the “no feedback” run was a fairly extreme outlier. However, for the SFMS we find that the “no feedback” run produces results consistent with the bulk of our feedback model simulations.

A similar set of conclusions holds for the redshift  $z = 1$  and  $z = 0$  SFMS. From redshift  $z = 2$  to  $z = 1$  and redshift  $z = 1$  to  $z = 0$  there is a significant decrease in the normalisation of the observed and simulated SFMS. How-

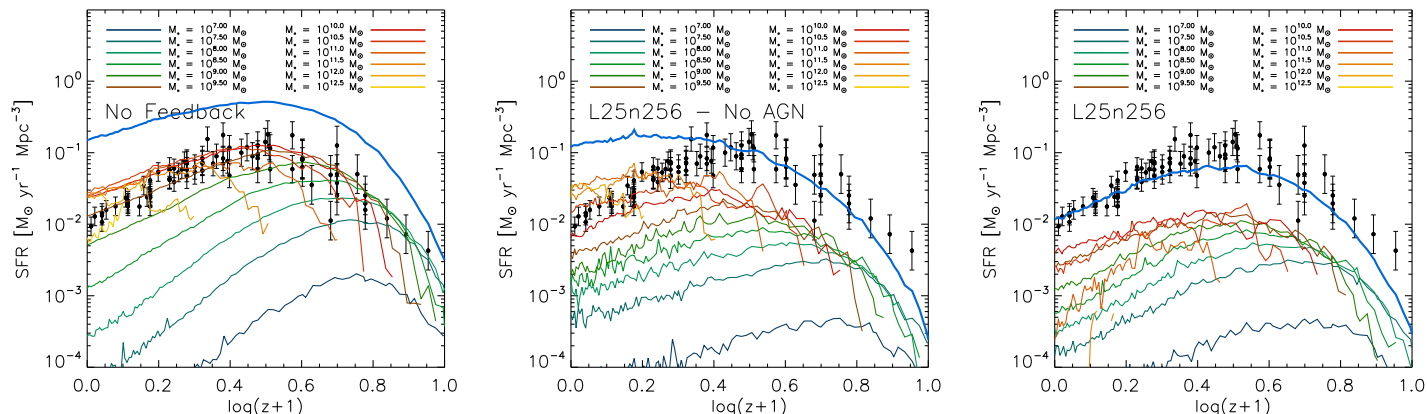


**Figure 6.** Cosmic star formation rate density is as a function of redshift (blue thick line) along with a collection of observational constraints compiled in Behroozi et al. (2012). The three panels show the “no feedback” simulation (left), the standard model with AGN feedback turned off (center), and the fiducial L25n256 model (right). As noted in the legend, contributions to the SFR density from various galaxy mass bins are shown. We note that at early times, the shape of the SFR density evolution is dominated by the most massive galaxies while at late times the decline in the SFR density is determined by the suppression of star formation via AGN feedback in the most massive haloes. Star formation driven winds regulate the SFR density at early times, while AGN feedback is critical past redshift  $z = 2$ .

ever, the redshift  $z = 1$  and  $z = 0$  simulated SFMS relations are still at or below the observed relations and have slopes (near unity) which are steeper than observations. This trend can be seen more explicitly in Figure 8, which shows the median specific star formation rate evolution for galaxies in the mass bin  $10^{9.75} M_{\odot} < M_{*} < 10^{10.25} M_{\odot}$  along with the observational data listed in Dutton et al. (2010). We find good agreement between the late time decline in the specific SFR normalization in the simulations and observations. Feedback (in particular, galactic winds) plays a role in determining the normalisation of this relation. Stronger star formation driven winds lead to higher SFMS normalisations. This trend – which can be seen in both Figures 7 and 8 – is driven by two effects: (i) strong winds suppress the stellar mass growth of galaxies, moving them “to the left” in Figure 7 and (ii) by reducing star formation in low mass systems, strong winds increase the amount of star forming gas that is available to more massive systems at later times. The second of these points can also be seen as an increase in the bright end on the luminosity function shown in Figure 4. However, most of the feedback models show the same overall trend with redshift, which is driven by the reduction in the accretion rate with redshift which scales roughly as  $\dot{M}_{\text{acc}} \propto (1+z)^{2.25}$  (Birnboim et al. 2007; Genel et al. 2008; Dutton et al. 2010).

The resolution dependence of these results is demonstrated in the top panel of Figure 7 where we show the SFMS for our fiducial feedback model at three different resolutions and the left panel of Figure 8 which shows the SFMS normalisation evolution for the same simulations. There is a weak resolution dependence in the derived SFMSs. This is especially true for the intermediate and high mass SFMS relations, which are nearly identical at all plotted redshifts.

We conclude that our galaxy formation model predicts a star formation main sequence which is in reasonable agreement with the observations. This result is similar to that found in other recent studies (e.g., Davé et al. 2011b; Puch-

wein & Springel 2013; Kannan et al. 2013). Generally, simulations have difficulties obtaining a SFMS with a slope substantially shallower than unity and often have SFMSs that are mildly depressed in their normalisation relative to observations. Neither of these issues can be easily corrected without introducing problems in the simulated GSMF – especially at the low mass end. The offset between the simulated and observational SFMS is fairly minor, but it should be noted that improving the agreement here would give rise to tension in other observationally constrained relations.

## 5 GALAXY PROPERTIES

The previous two sections focused on examining the buildup of stellar mass in our simulations. We have shown that our feedback models are capable of producing galaxy populations that form and evolve over time consistently with a wide range of observational constraints. In this section, we explore the simulated Tully-Fisher and mass-metallicity relations.

### 5.1 Tully-Fisher

The Tully-Fisher (TF) relation describes the observed correlation between galactic mass (or luminosity) and rotational velocity (Tully & Fisher 1977). This is an important indicator of galactic structure because it combines information about galactic mass, concentration, and angular momentum. It is a major goal of galaxy formation models to explain the slope, zero-point, scatter, and redshift evolution of the TF relation (e.g. Silk 1997; Steinmetz & Navarro 1999; van den Bosch 2000, 2002; Sommer-Larsen et al. 2003; Dutton et al. 2007). We showed already in Paper I, that our galaxy formation model reproduces the  $z = 0$  TF relations. In this section, we examine the TF relation at several redshifts and

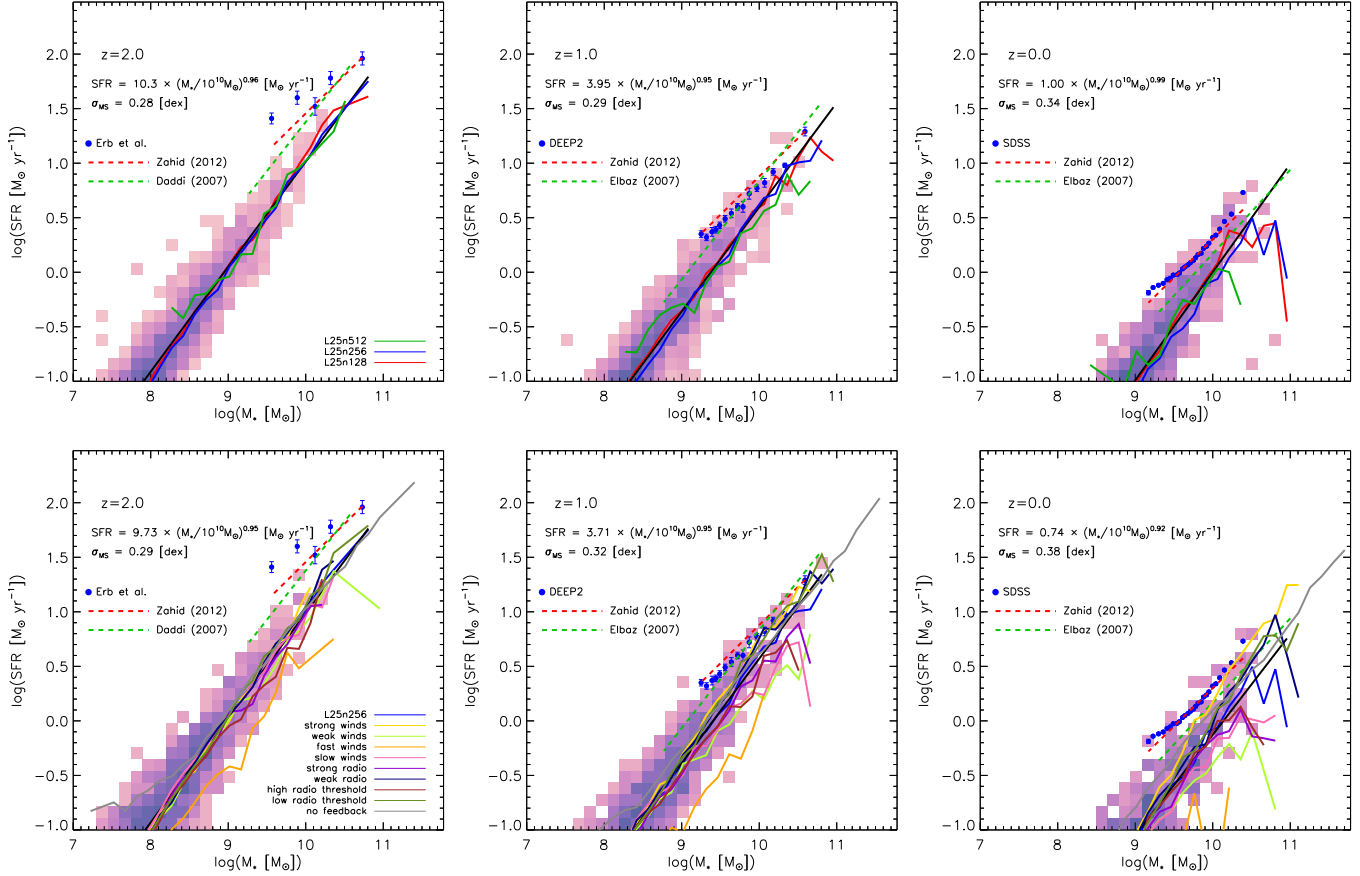


**Figure 7.** Binned median star formation main sequence relations are shown for three different resolutions (top) and our varied feedback models (bottom) as solid lines for redshifts  $z = 2$ ,  $z = 1$ , and  $z = 0$  from left to right, respectively. In the background, two dimensional histograms show the galaxy distribution for the L25n512 (top) and L25n256 (bottom) simulations. The dark solid line shows the linear best fit to the simulated star formation main sequence relation, with the best fit parameters noted within the plotted region. For comparison, we show the appropriate observational data taken from SDSS DR7 (Abazajian et al. 2009), DEEP2 (Davis et al. 2003), and Erb et al. (2006) at redshifts  $z = 0$ , 0.8, and 2 as compiled in Table 1 of Zahid et al. (2012), along with best fit SFMS relations from Elbaz et al. (2007) and Daddi et al. (2007).

explore how our model evolves with respect to observational constraints.

Figure 9 shows the Tully-Fisher relations for the various feedback models at redshifts  $z = 2$ ,  $z = 1$ , and  $z = 0$ . We show the binned median Tully-Fisher relation for the various feedback models (bottom) and resolutions (top) along with a two dimensional histogram denoting the distribution of galaxies for the “L25n256” (bottom) and “L25n512” (top) simulations. For comparison, observational Tully-Fisher relations are also shown.

The simulated galaxy populations do contain positive correlations between the galaxy stellar mass and  $V_{\text{max}}$ . To parameterise our results, we adopt a functional form for the TF relation

$$\log \left( \frac{V_{\text{max}}}{\text{km sec}^{-1}} \right) = \log \left( \frac{V_{\text{max},10}}{\text{km sec}^{-1}} \right) + b \log \left( \frac{M_*}{10^{10} M_\odot} \right) \quad (2)$$

where  $M_*$  is the stellar mass, and  $V_{\text{max}}$  is the circular velocity at twice the stellar half mass radius. A best fit relation is found at each redshift via RMS minimisation of all galaxies with stellar masses  $10^9 M_\odot < M_* < 10^{11} M_\odot$ . The best fit is plotted within Figure 9 as a solid black line and the param-

eters are printed within the plotted region for the “L25n256” (bottom) and “L25n512” (top) simulations.

Feedback is required to obtain a proper slope and normalisation for the Tully-Fisher relation at any of the plotted redshifts, as seen in the bottom panel of Figure 9. The simulated “no feedback” Tully-Fisher relation is too steep and extends to substantially higher rotational velocities than are seen observationally. Most of the feedback models produce consistent Tully-Fisher relation slopes, but there is some variability in the normalisation as has been discussed already in Paper I. At redshift  $z = 0$  the L25n256 simulation  $M_* - V_{\text{max}}$  relation has a slope of  $b = 0.22$  which is similar to the local TF relation slope found by Bell & de Jong (2001,  $b \approx 0.23$ ) and slightly below the more recent measurements of Reyes et al. (2011,  $b = 0.27$ ). As we consider the evolution to higher redshift, the L25n256 simulation retains a nearly constant  $M_* - V_{\text{max}}$  relation slope of  $b = 0.22 - 0.23$ , which is reasonably consistent with the observed redshift  $z = 1$  TF slope (Miller et al. 2012,  $b = 0.26$ ). Although we do not list their slopes explicitly, the other feedback models explored here all yield similar slopes (with the exception of the “no feedback” simulation).



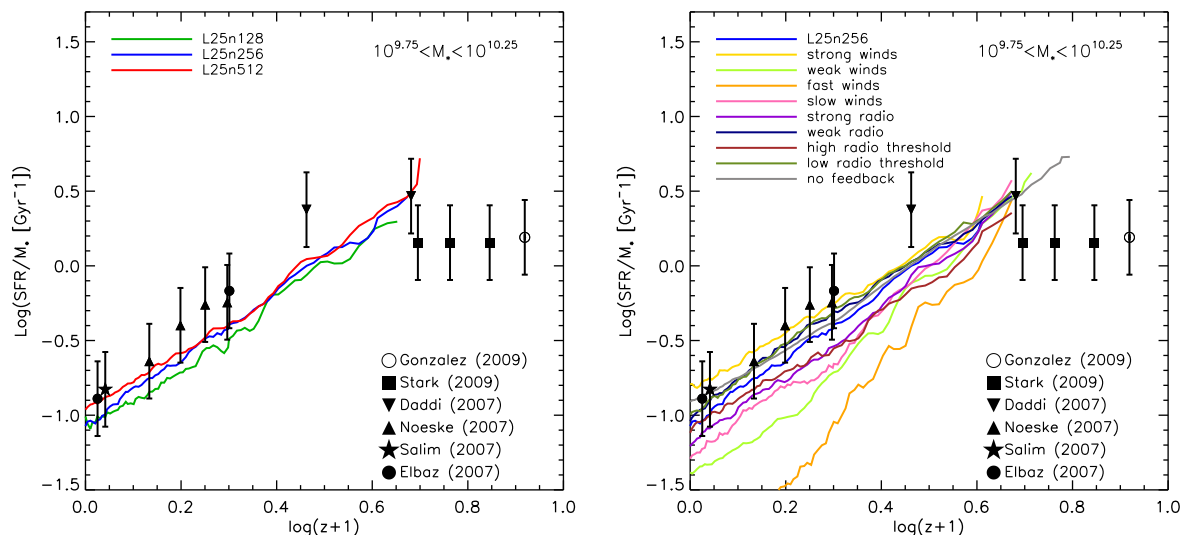


**Figure 8.** The median specific star formation rate for galaxies with stellar masses  $10^{9.75} M_{\odot} < M_{*} < 10^{10.25} M_{\odot}$  is shown as a function of redshift along with observational data for three different resolutions of our fiducial feedback model (left) and variations of our fiducial feedback model parameters (right). There is a clear evolution toward higher specific star formation rates in the past as seen in the data. Feedback – particularly our wind model – is partially responsible for the normalisation of this relation. There is a normalization offset between the models and the observations, which slowly increases with time.

All of feedback simulations show a slight evolution in the normalisation of the Tully-Fisher relation towards higher rotational velocities at a fixed stellar mass at higher redshifts. Since this evolution is somewhat subtle (compared to e.g., the SFMS evolution), we have included the redshift  $z = 0$  TF relation in all redshift plots. The normalisation evolution is similar to that found in high redshift disk-dominated samples (e.g., Miller et al. 2013; Cresci et al. 2009). We note that while a number of previous studies have indicated that there is an offset in the high redshift TF relation relative to the local TF relation that increases with redshift (Puech et al. 2008; Cresci et al. 2009; Gnerucci et al. 2011; Vergani et al. 2012; Miller et al. 2013), there is also evidence suggesting that no such evolution occurs in the TF normalisation (Miller et al. 2011, 2012). It is unclear exactly what drives the discrepancy in the observed normalisation evolution. However, one possibility is that the offset is sensitive to galaxy morphology (Miller et al. 2013) which could explain why the rotationally dominated selected samples (e.g., Cresci et al. 2009) found clear TF relation offsets.

The resolution dependence of these inferences can be seen in the top panel of Figure 9 where we show the simulated Tully-Fisher relation for our fiducial feedback model at three different resolutions. There is a noticeable offset between the low and intermediate resolution simulations at all redshifts, with the intermediate resolution simulation having lower rotational velocities at a fixed stellar mass. The magnitude of this offset decreases between the intermediate and high resolution simulations, and is particularly small for the most massive systems at all redshifts. This indicates that the simulated Tully-Fisher relation is numerically converging for our highest resolution simulations. Moreover, we note that the highest resolution simulations are converging to a Tully-Fisher relation which is consistent with the marked

observational relations at all redshifts. While the measured slope of the simulated intermediate resolution simulation remained fixed at  $b = 0.22 - 0.23$  over the plotted redshift range, the slope of the high resolution simulation remains nearly fixed at a slightly larger value of  $b = 0.24 - 0.26$  – which is still consistent with the local and high redshift measured TF slopes.

Overall, we find that our fiducial feedback galaxy formation model describes the evolution of the slope and normalisation of the stellar TF relation reasonably well (certainly much better than our model without feedback). Our results are consistent with the conclusions of several previous simulation based studies that examined the local Tully-Fisher relation (e.g., Portinari & Sommer-Larsen 2007; Croft et al. 2009; de Rossi et al. 2010, 2012; McCarthy et al. 2012b). Typically, it is found that including feedback is critical to obtaining the correct TF normalisation (e.g., Governato et al. 2007) because it reduces buildup of stellar material in a central, compact component. We do not find any significant evolution in the slope of the TF relation with redshift, but we do find an evolution in the normalisation which is consistent with both observational results and previous simulation work (de Rossi et al. 2010).

## 5.2 Mass Metallicity Relation

After metals are returned to the ISM from aging stellar populations, they can be retained in the ISM, locked into future generations of stars, or ejected from the galaxy via outflow processes driven by stellar winds or AGN activity. Although not all of these processes are directly observable, HII region nebular emission line diagnostics allow for observational estimates of the metallicity of star-forming gas in galaxies. This provides information that can constrain the character

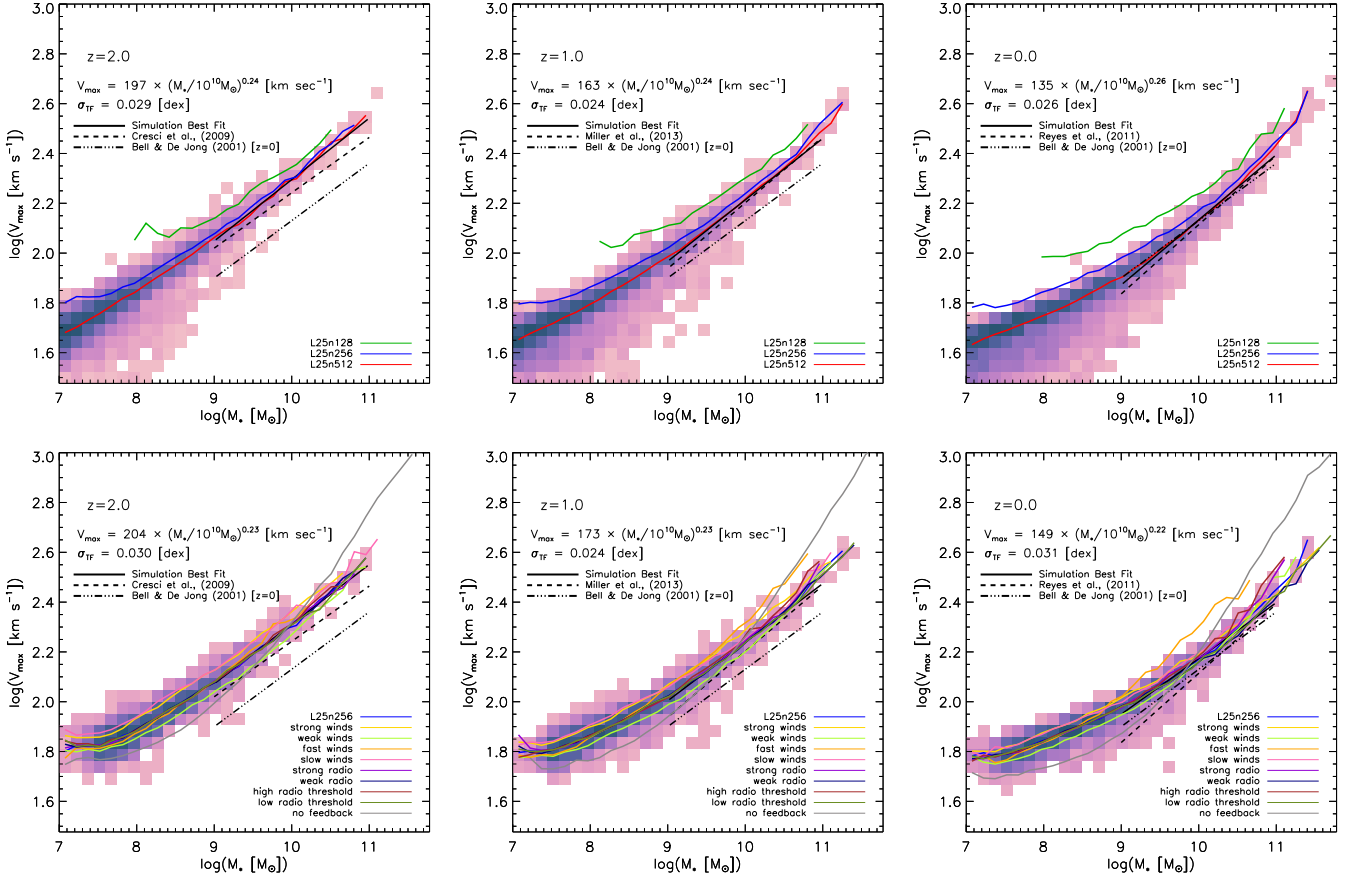


**Figure 9.** Binned median Tully-Fisher relations are shown for three different resolutions (top) and our varied feedback models (bottom) as solid lines for redshifts  $z = 2$ ,  $z = 1$ , and  $z = 0$  from left to right, respectively. In the background, two dimensional histograms show the galaxy distribution for the L25n512 (top) and L25n256 (bottom) simulations. The dark solid line shows the best fit to the simulated TF relation with the best fit parameters noted within the plotted region for the L25n512 (top) and L25n256 (bottom) simulations.

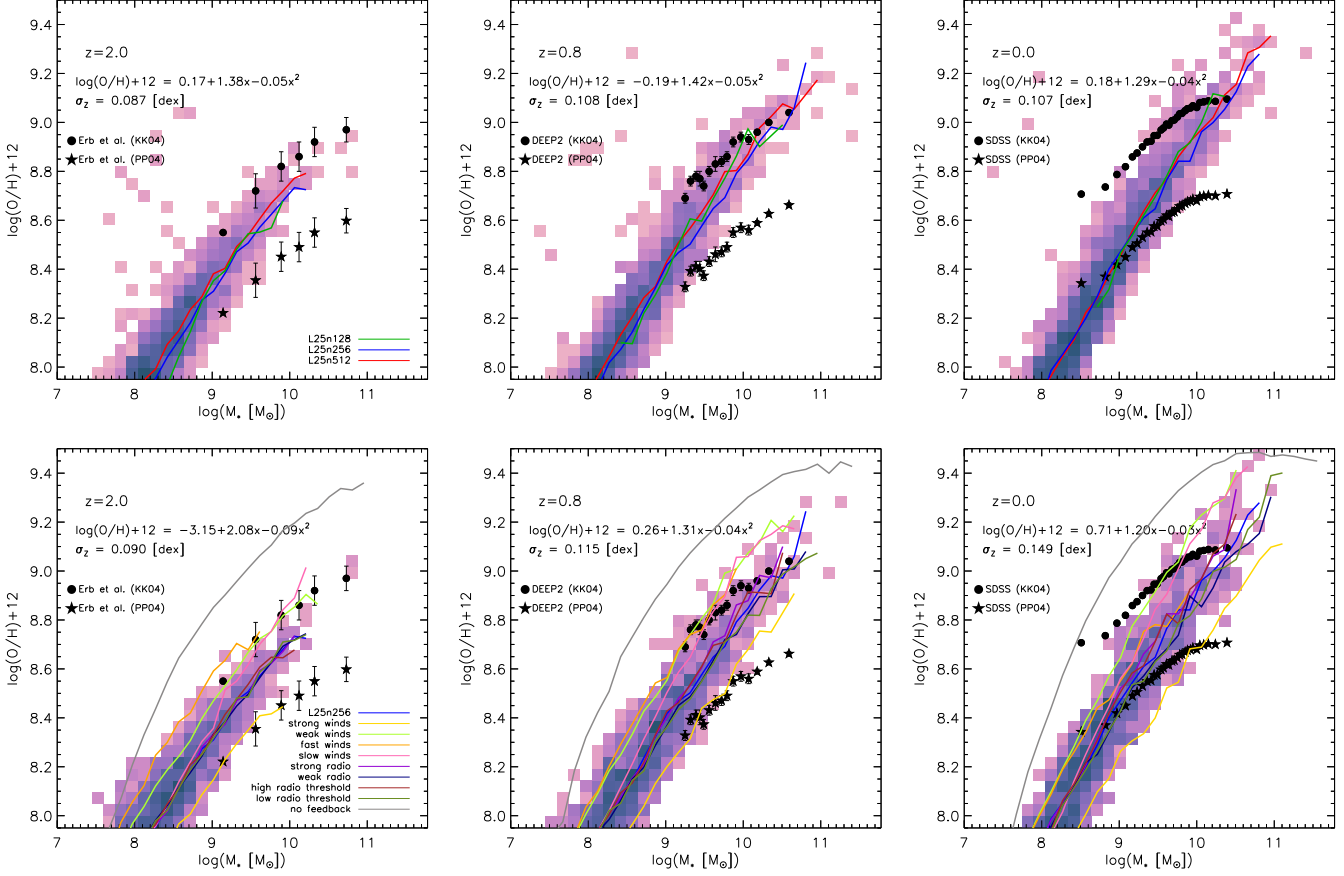
of outflow models. Although it is critical to many of the results presented in the previous sections that strong winds must operate on low mass galaxies in order for their stellar mass build-up to mimic observations, these same winds will carry metals along with them and can potentially deplete a substantial fraction of a galaxy’s metal content. On the other hand, in the absence of any strong feedback we expect that galaxies will be unable to eject any metals which they produce, potentially leading to an overproduction of metals.

Figure 10 shows the MZ relations for our various feedback models at redshifts  $z = 2$ ,  $z = 1$ , and  $z = 0$ . The metallicities have been determined by finding the average star formation rate weighted oxygen abundance in each galaxy, which places an emphasis on star-forming gas as is done through metallicity estimates via nebular emission lines. In each figure, we show a two-dimensional histogram denoting the distribution of galaxies for the “L25n256” (bottom panel) and “L25n512” (top panel) simulations. Additionally, we show coloured lines marking the binned median MZ relation for the various feedback models (bottom) and resolutions (top) as noted in the legend. Observational MZ relations are shown within the figures for comparison. We include MZ data from SDSS DR7 (Abazajian et al. 2009), DEEP2 (Davis et al. 2003), and Erb et al. (2006) at redshifts  $z = 0, 0.8$ , and 2 as compiled in Table 1 of Zahid

et al. (2012) for comparison against the simulation results. There are uncertainties in the overall normalisation of the observed metallicity abundance measurements, so we apply the empirical conversion of Kewley & Ellison (2008) and plot the observed MZ data using the Kobulnicky & Kewley (2004, hereafter: KK04) and Pettini & Pagel (2004, hereafter: PP04) diagnostics.

The metal content of galaxies is strongly dependent on the adopted feedback model, as demonstrated in the bottom panel of Figure 10. At redshift  $z = 2$ , all of the models (except for the “no feedback” case) produce MZ relations that are fairly similar in shape. There is some dispersion in their normalisations. Simulations with strong feedback are efficient at ejecting metals out of galaxies, and tend to have lower MZ relation normalisations. Conversely, simulations with weak winds tend to have higher MZ relation normalisations. At the low mass end, the offset between the “strong winds” and “weak winds” simulations is about 0.3 dex, with the fiducial feedback model (L25n256) falling right in-between. Changes in the AGN feedback do not have a major impact on the high redshift MZ relation. In any case, at redshift  $z = 2$  all of the feedback models fall between in the PP04 and KK04 measured MZ relations, and so we cannot rule out any of the models clearly (except for the “no feedback” case).





**Figure 10.** Binned median mass-metallicity relations are shown for three different resolutions (top) and our varied feedback models (bottom) as solid lines for redshifts  $z = 2$ ,  $z = 1$ , and  $z = 0$  from left to right, respectively. In the background, two dimensional histograms show the galaxy distribution for the L25n512 (top) and L25n256 (bottom) simulations. The observational MZ relations are taken from SDSS DR7 (Abazajian et al. 2009), DEEP2 (Davis et al. 2003), and Erb et al. (2006) as compiled in Table 1 of Zahid et al. (2012). We show the observational MZ relations using the KK04 diagnostic, as well as the PP04 diagnostic, to demonstrate systematic uncertainties in observational nebular emission line determinations.

At redshift  $z = 0.8$ , the observed MZ relation has shifted slightly upward toward higher metallicities at all mass scales. Many of the feedback simulations show a similar shift. However, the simulations evolve toward higher metallicities preferentially for massive systems, which steepens the simulated MZ relation relative to the observed relation. As a result, all of the feedback runs now have slopes that are slightly steeper than the observed relations. Two of the runs (“weak winds” and “slow winds”) are well in excess of the observed KK04 MZ relation. Most of the other runs, however, are still situated between the PP04 and KK04 observational relations. Overall, the most notable missing feature from the simulated MZ relation is the flattening of the MZ relation for some of the more massive systems. While the observed MZ relation flattens for basically all metallicity diagnostics at all observed redshifts, our simulated MZ relation does not show a similar behaviour.

At redshift  $z = 0$ , the simulated MZ relation is now clearly distinct in shape from the observed MZ relation. The three main descriptive features of the observed MZ relations are the low mass slope, the high mass flattening, and the overall normalisation. None of the feedback models accurately reproduce the low mass slope or the high mass

flattening. Instead, most of the feedback models produce a constant slope MZ relation that is steeper than the observed relation. There remains a clear dispersion in the normalisation of the MZ relation for the various feedback models. Most of the models lie between the PP04 and KK04 MZ relations in the galaxy mass range  $10^9 M_\odot < M_* < 10^{10} M_\odot$ . However, owing to their steep slopes, most of the models have both insufficiently low metallicity galaxies at the low mass end and overly enriched galaxies at the high mass end.

The resolution dependence of the simulated MZ relation can be seen in the upper panel of Figure 10. There are no major or systematic changes in the simulated MZ relation between the different resolution simulations. This consistency holds true for all of the plotted redshifts, indicating that the MZ relation is well converged. Any issues with the shape of the simulated MZ relation are not likely to substantially change if we moved to higher resolution simulations.

The origin of the steep MZ slope in our simulations is the low metal retention efficiency of low mass galaxies owing to galactic winds with large mass loadings. Strong winds facilitate the mixing of the central metal rich disk gas with the metal poor hot halo gas. In low mass galaxies – where the mass loading factors for winds are very high – this prevents

a substantial buildup of metal mass, which ultimately leads to the steep redshift  $z = 0$  MZ relation shown in Figure 10. We note that this effect is stronger if we do not treat the mass and metal loading for our winds independently. As described above and in Paper I, we have adopted a wind metal loading factor in our model, which determines the metallicity of the wind material relative to the local ISM metallicity from where the wind is launched. Even with a reduced metal loading factor, which helps galaxies maintain a larger fraction of the metals they produce, we still find that the lowest mass galaxies have gas-phase metallicities that are at or below the lowest of observational expectations. This exposes an interesting tension between our need for high wind efficiencies to reduce the buildup of stellar mass in low mass galaxies, and the need for low mass galaxies to be relatively efficient at retaining their metal content (Zahid et al. 2012). The solution to this tension likely either lies in: (i) fundamentally reducing the accretion efficiency of low mass galaxies via some feedback mechanism that is able to disrupt and heat the IGM around these systems or (ii) a more detailed wind model that self consistently handles the entrainment of low metallicity material as winds propagate out of galaxies (e.g., Hopkins et al. 2012a).

We conclude that many of our feedback models are capable of producing an MZ relation which has an appropriate slope and normalisation at high redshift, but is notably steeper than observations at low redshift (albeit with reasonable normalisations). Several previous studies have been successful at reproducing the MZ relation at both redshift  $z = 0$  (e.g., Brooks et al. 2007; de Rossi et al. 2007) and higher redshifts (Brooks et al. 2007; Kobayashi et al. 2007; de Rossi et al. 2007; Tassis et al. 2008) and we note that the MZ results presented in this section are somewhat different from what has been found previously (in particular Davé et al. 2011a, which is of practical interest because of the similarities in our wind models). There are three principle sources of differences between our models and earlier ones, which are all numerical in nature.

First, the gas fractions of the galaxies formed in the simulations presented are generally higher than those of Davé et al. (2011a). This is partially due to differences in the way galaxies accrete gas (Nelson et al. 2013) and form central gas reservoirs (Torrey et al. 2012), which makes it difficult to separate out particular aspects of the calculations that lead to results that are different from ours. Higher gas fractions lead to diluted/lowered metallicity values, which is partially responsible for the lower metallicity values of low mass galaxies found in our simulations. Second, while mixing is numerically suppressed in SPH simulations, it can be artificially enhanced in grid based simulations due to poor resolution. Employing a moving mesh hydro solver minimises the impact of artificial mixing significantly (Springel 2010; Genel et al. 2013). Nevertheless, mixing in our simulations is more efficient than in previous SPH simulations, which will lead to a systematic lowering (or dilution via mixing) of the central galactic gas phase metallicity. Third, the wind prescriptions used in Davé et al. (2011a) are momentum conserving, which scale less steeply with galaxy mass than the energy conserving wind models adopted here. These effects translate into a shallower MZ relation, which would be in better agreement with the redshift  $z = 0$  observed MZ slope, as was found in Davé et al. (2011a). The overall pic-

ture observed in our simulations of mixing dominating the reduction in the observed metallicity of low mass systems is similar to that presented in Tassis et al. (2008), except in our case this process is too efficient to reproduce observations. This places constraints on the character of our wind model which will be considered in future work.

## 6 DISCUSSION AND CONCLUSIONS

Simulating the formation and evolution of the galaxy population in a fully cosmological context is an inherently difficult numerical task. It requires a very large dynamic range such that galactic structural scales can be resolved within a full cosmic volume simulation box. Furthermore, it requires numerically well-posed modelling of the complex baryon physical processes to yield realistic galaxy populations.

In Paper I we introduced a new feedback module into the simulation code AREPO which is intended to regulate the growth of galaxies by introducing star formation driven winds and AGN feedback. It was shown that – with this feedback module included – our simulations are able to match a number of redshift  $z = 0$  observed galaxy relations. The primary goal of this paper is to extend the work presented in Paper I by presenting a summary of high redshift galaxy properties as realised in a set of large-volume, high-resolution cosmological hydrodynamical simulations with varied assumptions for the star formation driven winds and AGN feedback.

The critical point of including feedback in our models is to regulate when and where galaxies build up their stellar mass. The performance of any such model can be directly tested by comparing against observations at several epochs. As we have attempted to demonstrate throughout this paper, we have constructed a reasonably self-consistent model, where galactic stellar mass measurements, star formation rate measurements, and even structural measurements are reproduced by our fiducial feedback model without major violations of observational constraints. However, our implementation of feedback is not unique, and it is worth discussing some of the more subtle tensions that exist in our models that might provide information about how we can improve upon them in the future.

Our currently implemented star formation driven wind prescription is based on the kinetic wind model of Springel & Hernquist (2003a) with a modification to allow for variable wind speeds based on the local dark matter velocity dispersion (Oppenheimer & Davé 2006; Okamoto et al. 2010). In our models, these winds are critical for reproducing the evolving low mass slope of the GSMF and regulating the magnitude of global star formation rate density in low mass haloes in the early Universe. The two free parameters in this model (the energy normalisation and the wind speed) have been set based on their ability to reproduce the evolving SFRD and redshift  $z = 0$  GSMF (and, similarly, the redshift  $z = 0$  SMHM relation). By examining the evolution of low mass galaxies, we found there is an overproduction of stellar mass in these systems at early times compared to current observational standards as shown in Figure 1 as well as in Figure 5. This offset cannot be fully corrected by simply introducing a larger energy normalisation for our wind model because of the characteristic flat evolution in the number

density of low mass systems in all of our feedback model simulations at late times.

Similarly all of our simulations tend to mildly undershoot the observed SFMS normalisation with a slope that is systematically steeper than SFMS observational measurements. This makes the disagreement between our simulations and observations the worst for low mass galaxies. Introducing stronger winds does tend to increase the normalisation of the SFMS. However, the normalisation shift is most pronounced at late times (after previously ejected wind material has had time to re-accrete), while the normalisation offset between observations and simulations is most dramatic at high redshift (i.e.  $z = 2$ ).

Nevertheless, our fiducial feedback model matches a wide range of observational metrics. We note that our model only slightly overshoots in the mass buildup of low mass galaxies (by a factor of  $\sim 2$ ) and only slightly undershoots the observed star formation rates of low mass galaxies (by, again, a factor of  $\sim 2$ ). Given that observational uncertainties on, e.g., stellar mass measurements (Mitchell et al. 2013) or star formation rate determinations can be of this same order, we would not stress this as being a critical issue to our model. However, we emphasise that within the context of our adopted kinetic wind model there are not any immediate or clear alternative parameter choices that will allow us to simultaneously reduce these tensions further.

One clue regarding the nature of our wind model can be obtained from comparisons with observed MZ relations. The large wind mass loading factors that are required to regulate the growth of low mass systems double back as very efficient mechanisms to eject metals from galaxies. This gives rise to an important, yet seemingly unappreciated, tension. Empirical estimates of the total oxygen content of low mass galaxies indicate that these systems can eject only some reasonably small fraction (e.g., 30%) of their metals (Zahid et al. 2012). Yet, when cosmological simulations tune their wind prescriptions to match, e.g., the galaxy stellar mass function, they often adopt very strong wind mass loading factors that substantially exceed this limit under the traditional assumption that the metallicity of wind material is the same as the metallicity of the local ISM from where the wind was launched.

There are two clear ways to resolve this issue. The first is to reduce the efficiency with which material is ejected out of galaxies. This can be achieved very straightforwardly in our models by lowering the energy normalisation for our winds. However, doing so would immediately increase the masses of all galaxies, ruining the agreement with the GSMF, SMHM relation, and early SFRD evolution. A more robust solution would be to allow winds to have a more disruptive effect on the accretion of gas into low mass galaxies. By, for example, allowing winds to be pushed by cosmic ray streaming (Uhlir et al. 2012) or to carry along with them some thermal energy, it may be possible to reduce the star formation rates in low mass galaxies by disrupting the IGM around these systems. The second possible solution is to modify our sub-grid picture for the wind structure, as we have done in this paper. Substantially higher resolution simulations on the origin of galactic winds indicate that: (i) wind mass loading factors far in excess of unity are physically plausible and (ii) the origin and composition of ejected material can depend on the physical mechanism responsible for launching

the wind (Hopkins et al. 2012a). By accounting for the impact of low metallicity gas entrainment that might occur as a wind propagates out of the systems, the evolution of the MZ relation can be brought back into reasonable agreement with observations. It is likely that both of these issues are partially responsible for the MZ relation tension, and it will be interesting to consider how alternative galactic wind formulations and modifications of our currently employed hydrodynamically decoupled wind prescriptions can resolve this issue.

The most promising next step to be taken with these models is to extend their application to larger simulation volumes at comparable mass and spatial resolution to the runs we have employed here. The  $L = 25h^{-1}$  Mpc boxes used in this paper have served as excellent testbeds for understanding the impact of our feedback models. Within these volumes we can already find a wide variety of galaxy properties and demonstrate the success of our model in reproducing basic observational constraints like the GSMF and cosmic SFRD. However, this (relatively small) simulation box does not do an adequate job of sampling different density environments or of producing a sufficiently large number of massive galaxies, groups, and clusters to perform detailed statistical modelling. For this reason, our ability to discuss the high redshift cutoff the GSMF or the turnover in the SMHM relation is limited. Moreover, our ability to do detailed morphological classification and perform environment studies is limited. This can be remedied by moving to larger simulation volumes (ideally without sacrificing mass or spatial resolution). Using larger simulation volumes, many additional science questions can be addressed including correlations between galactic star formation rate and environment, correlations between galactic morphology and physical properties, or the predominant formation venues for massive elliptical and star forming disk galaxies.

## ACKNOWLEDGEMENTS

We thank Greg Snyder, Dylan Nelson, Dave Patton, Sara Ellison, Lisa Kewley, Jabran Zahid, and Giovanni Cresci for helpful suggestions on this work. MV acknowledges support from NASA through Hubble Fellowship grant HST-HF-51317.01. VS acknowledges support from the European Research Council under ERC-StG grant EXAGAL-308037. LH acknowledges support from NASA through grant NNX12AC67G.

## REFERENCES

- Abazajian, K. N., Adelman-McCarthy, J. K., Agüeros, M. A., et al. 2009, *ApJS*, 182, 543
- Baldry, I. K., Glazebrook, K., & Driver, S. P. 2008, *MNRAS*, 388, 945
- Balogh, M. L., Pearce, F. R., Bower, R. G., & Kay, S. T. 2001, *MNRAS*, 326, 1228
- Behroozi, P. S., Wechsler, R. H., & Conroy, C. 2012, *ArXiv e-prints*, 1207.6105
- Bell, E. F., & de Jong, R. S. 2001, *ApJ*, 550, 212
- Birnboim, Y., Dekel, A., & Neistein, E. 2007, *MNRAS*, 380, 339

- Booth, C. M., & Schaye, J. 2009, *MNRAS*, 398, 53
- Bouwens, R. J., Illingworth, G. D., Franx, M., & Ford, H. 2008, *ApJ*, 686, 230
- Bouwens, R. J., Illingworth, G. D., Bradley, L. D., et al. 2009, *ApJ*, 690, 1764
- Bouwens, R. J., Illingworth, G. D., Oesch, P. A., et al. 2011, *ApJ*, 737, 90
- Bower, R. G., Benson, A. J., & Crain, R. A. 2012, *MNRAS*, 422, 2816
- Boylan-Kolchin, M., Springel, V., White, S. D. M., Jenkins, A., & Lemson, G. 2009, *MNRAS*, 398, 1150
- Brooks, A. M., Governato, F., Booth, C. M., et al. 2007, *ApJ*, 655, L17
- Bruzual, G., & Charlot, S. 2003, *MNRAS*, 344, 1000
- Chabrier, G. 2003, *PASP*, 115, 763
- Charlot, S., & Fall, S. M. 2000, *ApJ*, 539, 718
- Chartas, G., Brandt, W. N., Gallagher, S. C., & Garmire, G. P. 2002, *ApJ*, 579, 169
- Conroy, C., & Wechsler, R. H. 2009, *ApJ*, 696, 620
- Conroy, C., Wechsler, R. H., & Kravtsov, A. V. 2006, *ApJ*, 647, 201
- Crain, R. A., Theuns, T., Dalla Vecchia, C., et al. 2009, *MNRAS*, 399, 1773
- Cresci, G., Hicks, E. K. S., Genzel, R., et al. 2009, *ApJ*, 697, 115
- Croft, R. A. C., Di Matteo, T., Springel, V., & Hernquist, L. 2009, *MNRAS*, 400, 43
- Croton, D. J., Springel, V., White, S. D. M., et al. 2006, *MNRAS*, 365, 11
- Cucciati, O., Tresse, L., Ilbert, O., et al. 2012, *A&A*, 539, A31
- Daddi, E., Dickinson, M., Morrison, G., et al. 2007, *ApJ*, 670, 156
- Dalla Vecchia, C., & Schaye, J. 2008, *MNRAS*, 387, 1431
- Danovich, M., Dekel, A., Hahn, O., & Teyssier, R. 2012, *MNRAS*, 422, 1732
- Davé, R., Finlator, K., & Oppenheimer, B. D. 2011a, *MNRAS*, 416, 1354
- Davé, R., Oppenheimer, B. D., & Finlator, K. 2011b, *MNRAS*, 415, 11
- Davidzon, I., Bolzonella, M., Coupon, J., et al. 2013, *ArXiv e-prints*, 1303.3808
- Davis, M., Faber, S. M., Newman, J., et al. 2003, in *Society of Photo-Optical Instrumentation Engineers (SPIE) Conference Series*, Vol. 4834, Society of Photo-Optical Instrumentation Engineers (SPIE) Conference Series, ed. P. Guhathakurta, 161–172
- de Rossi, M. E., Tissera, P. B., & Pedrosa, S. E. 2010, *A&A*, 519, A89
- . 2012, *A&A*, 546, A52
- de Rossi, M. E., Tissera, P. B., & Scannapieco, C. 2007, *MNRAS*, 374, 323
- Debuhr, J., Quataert, E., & Ma, C.-P. 2011, *MNRAS*, 412, 1341
- Dekel, A., & Silk, J. 1986, *ApJ*, 303, 39
- Di Matteo, T., Colberg, J., Springel, V., Hernquist, L., & Sijacki, D. 2008, *ApJ*, 676, 33
- Di Matteo, T., Springel, V., & Hernquist, L. 2005, *Nature*, 433, 604
- Dubois, Y., Devriendt, J., Slyz, A., & Teyssier, R. 2012, *MNRAS*, 420, 2662
- Dubois, Y., & Teyssier, R. 2008, *A&A*, 477, 79
- Dutton, A. A., van den Bosch, F. C., & Dekel, A. 2010, *MNRAS*, 405, 1690
- Dutton, A. A., van den Bosch, F. C., Dekel, A., & Courteau, S. 2007, *ApJ*, 654, 27
- Elbaz, D., Daddi, E., Le Borgne, D., et al. 2007, *A&A*, 468, 33
- Erb, D. K., Shapley, A. E., Pettini, M., et al. 2006, *ApJ*, 644, 813
- Faber, S. M., Willmer, C. N. A., Wolf, C., et al. 2007, *ApJ*, 665, 265
- Faucher-Giguère, C.-A., Lidz, A., Hernquist, L., & Zaldarriaga, M. 2008a, *ApJ*, 688, 85
- Faucher-Giguère, C.-A., Lidz, A., Zaldarriaga, M., & Hernquist, L. 2009, *ApJ*, 703, 1416
- Faucher-Giguère, C.-A., Prochaska, J. X., Lidz, A., Hernquist, L., & Zaldarriaga, M. 2008b, *ApJ*, 681, 831
- Ferland, G. J., Korista, K. T., Verner, D. A., et al. 1998, *PASP*, 110, 761
- Ferland, G. J., Porter, R. L., van Hoof, P. A. M., et al. 2013, *ArXiv e-prints*, 1302.4485
- Few, C. G., Gibson, B. K., Courty, S., et al. 2012, *A&A*, 547, A63
- Font, A. S., McCarthy, I. G., Crain, R. A., et al. 2011, *MNRAS*, 416, 2802
- Fosalba, P., Gaztañaga, E., Castander, F. J., & Manera, M. 2008, *MNRAS*, 391, 435
- Gabasch, A., Bender, R., Seitz, S., et al. 2004, *A&A*, 421, 41
- Gabor, J. M., Davé, R., Oppenheimer, B. D., & Finlator, K. 2011, *MNRAS*, 417, 2676
- Genel, S., Vogelsberger, M., Nelson, D., et al. 2013, *ArXiv e-prints*, 1305.2195
- Genel, S., Genzel, R., Bouché, N., et al. 2008, *ApJ*, 688, 789
- Giallongo, E., Salimbeni, S., Menci, N., et al. 2005, *ApJ*, 622, 116
- Gnerucci, A., Marconi, A., Cresci, G., et al. 2011, *A&A*, 528, A88
- Governato, F., Willman, B., Mayer, L., et al. 2007, *MNRAS*, 374, 1479
- Guo, Q., White, S., Angulo, R. E., et al. 2012, *ArXiv e-prints*, 1206.0052
- Guo, Q., White, S., Li, C., & Boylan-Kolchin, M. 2010, *MNRAS*, 404, 1111
- Guo, Q., White, S., Boylan-Kolchin, M., et al. 2011, *MNRAS*, 413, 101
- Hahn, O., Teyssier, R., & Carollo, C. M. 2010, *MNRAS*, 405, 274
- Hatton, S., Devriendt, J. E. G., Ninin, S., et al. 2003, *MNRAS*, 343, 75
- Heckman, T. M., Lehnert, M. D., Strickland, D. K., & Armus, L. 2000, *ApJS*, 129, 493
- Henriques, B., White, S., Thomas, P., et al. 2012, *ArXiv e-prints*, 1212.1717
- Hernquist, L., & Springel, V. 2003, *MNRAS*, 341, 1253
- Hopkins, A. M., & Beacom, J. F. 2006, *ApJ*, 651, 142
- Hopkins, P. F., Cox, T. J., Hernquist, L., et al. 2013a, *MNRAS*, 430, 1901
- Hopkins, P. F., Cox, T. J., Kereš, D., & Hernquist, L. 2008a, *ApJS*, 175, 390
- Hopkins, P. F., Hernquist, L., Cox, T. J., et al. 2006, *ApJS*, 163, 1

- Hopkins, P. F., Hernquist, L., Cox, T. J., & Kereš, D. 2008b, *ApJS*, 175, 356
- Hopkins, P. F., Hernquist, L., Cox, T. J., Robertson, B., & Krause, E. 2007a, *ApJ*, 669, 45
- . 2007b, *ApJ*, 669, 67
- Hopkins, P. F., Keres, D., Murray, N., et al. 2013b, *ArXiv e-prints*, 1301.0841
- Hopkins, P. F., Quataert, E., & Murray, N. 2012a, *MNRAS*, 421, 3522
- . 2012b, *MNRAS*, 421, 3488
- Ilbert, O., Tresse, L., Zucca, E., & et al. 2005, *A&A*, 439, 863
- Kang, X., Jing, Y. P., Mo, H. J., & Börner, G. 2005, *ApJ*, 631, 21
- Kannan, R., Stinson, G. S., Macciò, A. V., et al. 2013, *ArXiv e-prints*, 1302.2618
- Karakas, A. I. 2010, *MNRAS*, 403, 1413
- Karim, A., Schinnerer, E., Martínez-Sansigre, A., et al. 2011, *ApJ*, 730, 61
- Katz, N., Hernquist, L., & Weinberg, D. H. 1992, *ApJ*, 399, L109
- Katz, N., Weinberg, D. H., & Hernquist, L. 1996, *ApJS*, 105, 19
- Kauffmann, G., Colberg, J. M., Diaferio, A., & White, S. D. M. 1999, *MNRAS*, 303, 188
- Kawata, D., & Gibson, B. K. 2003, *MNRAS*, 340, 908
- . 2005, *MNRAS*, 358, L16
- Kennicutt, Jr., R. C. 1998, *ApJ*, 498, 541
- Kereš, D., Katz, N., Weinberg, D. H., & Davé, R. 2005, *MNRAS*, 363, 2
- Kereš, D., Vogelsberger, M., Sijacki, D., Springel, V., & Hernquist, L. 2012, *MNRAS*, 425, 2027
- Kewley, L. J., & Ellison, S. L. 2008, *ApJ*, 681, 1183
- Klypin, A. A., Trujillo-Gomez, S., & Primack, J. 2011, *ApJ*, 740, 102
- Kobayashi, C., Springel, V., & White, S. D. M. 2007, *MNRAS*, 376, 1465
- Kobulnicky, H. A., & Kewley, L. J. 2004, *ApJ*, 617, 240
- Komatsu, E., Smith, K. M., Dunkley, J., et al. 2011, *ApJS*, 192, 18
- Kurosawa, R., & Proga, D. 2009, *MNRAS*, 397, 1791
- Le Borgne, D., Rocca-Volmerange, B., Prugniel, P., et al. 2004, *A&A*, 425, 881
- Leitherer, C., Schaerer, D., Goldader, J. D., et al. 1999, *ApJS*, 123, 3
- Lilly, S. J., Le Fevre, O., Hammer, F., & Crampton, D. 1996, *ApJ*, 460, L1
- Madau, P., Pozzetti, L., & Dickinson, M. 1998, *ApJ*, 498, 106
- Marchesini, D., van Dokkum, P. G., Förster Schreiber, N. M., et al. 2009, *ApJ*, 701, 1765
- Marchesini, D., van Dokkum, P., Quadri, R., et al. 2007, *ApJ*, 656, 42
- Marchesini, D., Whitaker, K. E., Brammer, G., et al. 2010, *ApJ*, 725, 1277
- Martin, C. L. 2005, *ApJ*, 621, 227
- McCarthy, I. G., Font, A. S., Crain, R. A., et al. 2012a, *MNRAS*, 420, 2245
- McCarthy, I. G., Schaye, J., Font, A. S., et al. 2012b, *MNRAS*, 427, 379
- McCarthy, I. G., Schaye, J., Ponman, T. J., et al. 2010, *MNRAS*, 406, 822
- McGee, S. L., & Balogh, M. L. 2010, *MNRAS*, 403, L79
- McQuinn, M., Lidz, A., Zaldarriaga, M., et al. 2009, *ApJ*, 694, 842
- Miller, S. H., Bundy, K., Sullivan, M., Ellis, R. S., & Treu, T. 2011, *ApJ*, 741, 115
- Miller, S. H., Ellis, R. S., Sullivan, M., et al. 2012, *ApJ*, 753, 74
- Miller, S. H., Sullivan, M., & Ellis, R. S. 2013, *ApJ*, 762, L11
- Mitchell, P. D., Lacey, C. G., Baugh, C. M., & Cole, S. 2013, *ArXiv e-prints*, 1303.7228
- Mortlock, A., Conselice, C. J., Bluck, A. F. L., et al. 2011, *MNRAS*, 413, 2845
- Moster, B. P., Naab, T., & White, S. D. M. 2012, *ArXiv e-prints*, 1205.5807
- Moster, B. P., Somerville, R. S., Maubetsch, C., et al. 2010, *ApJ*, 710, 903
- Murali, C., Katz, N., Hernquist, L., Weinberg, D. H., & Davé, R. 2002, *ApJ*, 571, 1
- Murante, G., Giovalli, M., Gerhard, O., et al. 2007, *MNRAS*, 377, 2
- Murante, G., Arnaboldi, M., Gerhard, O., et al. 2004, *ApJ*, 607, L83
- Nelson, D., Vogelsberger, M., Genel, S., et al. 2013, *MNRAS*, 429, 3353
- Noeske, K. G., Weiner, B. J., Faber, S. M., & et, a. 2007, *ApJ*, 660, L43
- Ocvirk, P., Pichon, C., & Teyssier, R. 2008, *MNRAS*, 390, 1326
- Okamoto, T., Frenk, C. S., Jenkins, A., & Theuns, T. 2010, *MNRAS*, 406, 208
- Okamoto, T., Nemmen, R. S., & Bower, R. G. 2008, *MNRAS*, 385, 161
- Oppenheimer, B. D., & Davé, R. 2006, *MNRAS*, 373, 1265
- . 2008, *MNRAS*, 387, 577
- Oppenheimer, B. D., Davé, R., & Finlator, K. 2009, *MNRAS*, 396, 729
- Oppenheimer, B. D., Davé, R., Kereš, D., et al. 2010, *MNRAS*, 406, 2325
- Peng, Y.-j., Lilly, S. J., Kovač, K., et al. 2010, *ApJ*, 721, 193
- Pérez-González, P. G., Rieke, G. H., Villar, V., et al. 2008, *ApJ*, 675, 234
- Pettini, M., & Pagel, B. E. J. 2004, *MNRAS*, 348, L59
- Pierini, D., Maraston, C., Gordon, K. D., & Witt, A. N. 2005, *MNRAS*, 363, 131
- Poli, F., Giallongo, E., Fontana, A., et al. 2003, *ApJ*, 593, L1
- Portinari, L., Chiosi, C., & Bressan, A. 1998, *A&A*, 334, 505
- Portinari, L., & Sommer-Larsen, J. 2007, *MNRAS*, 375, 913
- Pounds, K. A., Reeves, J. N., King, A. R., et al. 2003, *MNRAS*, 345, 705
- Puchwein, E., & Springel, V. 2013, *MNRAS*, 428, 2966
- Puchwein, E., Springel, V., Sijacki, D., & Dolag, K. 2010, *MNRAS*, 406, 936
- Puech, M., Flores, H., Hammer, F., et al. 2008, *A&A*, 484, 173
- Rahmati, A., Pawlik, A. H., Raičević, M., & Schaye, J. 2013, *MNRAS*, 430, 2427
- Reeves, J. N., O'Brien, P. T., & Ward, M. J. 2003, *ApJ*,

- 593, L65
- Reyes, R., Mandelbaum, R., Gunn, J. E., Pizagno, J., & Lackner, C. N. 2011, *MNRAS*, 417, 2347
- Robertson, B., Bullock, J. S., Cox, T. J., et al. 2006, *ApJ*, 645, 986
- Robotham, A. S. G., & Driver, S. P. 2011, *MNRAS*, 413, 2570
- Rudick, C. S., Mihos, J. C., & McBride, C. 2006, *ApJ*, 648, 936
- Rujopakarn, W., Eisenstein, D. J., Rieke, G. H., et al. 2010, *ApJ*, 718, 1171
- Rupke, D. S., Veilleux, S., & Sanders, D. B. 2002, *ApJ*, 570, 588
- . 2005, *ApJS*, 160, 87
- Sales, L. V., Navarro, J. F., Theuns, T., et al. 2012, *MNRAS*, 423, 1544
- Salim, S., Rich, R. M., Charlot, S., et al. 2007, *ApJS*, 173, 267
- Salmi, F., Daddi, E., Elbaz, D., et al. 2012, *ApJ*, 754, L14
- Santini, P., Fontana, A., Grazian, A., et al. 2012, *A&A*, 538, A33
- Scannapieco, C., Tissera, P. B., White, S. D. M., & Springel, V. 2008, *MNRAS*, 389, 1137
- Scannapieco, C., Wadepuhl, M., Parry, O. H., et al. 2012, *MNRAS*, 423, 1726
- Schaye, J., Dalla Vecchia, C., Booth, C. M., et al. 2010, *MNRAS*, 402, 1536
- Schechter, P. 1976, *ApJ*, 203, 297
- Schiminovich, D., Ilbert, O., Arnouts, S., et al. 2005, *ApJ*, 619, L47
- Schmidt, M. 1959, *ApJ*, 129, 243
- Sijacki, D., & Springel, V. 2006, *MNRAS*, 366, 397
- Sijacki, D., Springel, V., Di Matteo, T., & Hernquist, L. 2007, *MNRAS*, 380, 877
- Sijacki, D., Springel, V., & Haehnelt, M. G. 2009, *MNRAS*, 400, 100
- Sijacki, D., Vogelsberger, M., Kereš, D., Springel, V., & Hernquist, L. 2012, *MNRAS*, 424, 2999
- Silk, J. 1997, *ApJ*, 481, 703
- Smolčić, V., Schinnerer, E., Zamorani, G., et al. 2009, *ApJ*, 690, 610
- Somerville, R. S., Hopkins, P. F., Cox, T. J., Robertson, B. E., & Hernquist, L. 2008, *MNRAS*, 391, 481
- Sommer-Larsen, J., Götz, M., & Portinari, L. 2003, *ApJ*, 596, 47
- Springel, V. 2010, *MNRAS*, 401, 791
- Springel, V., Di Matteo, T., & Hernquist, L. 2005a, *ApJ*, 620, L79
- . 2005b, *MNRAS*, 361, 776
- Springel, V., & Hernquist, L. 2003a, *MNRAS*, 339, 289
- . 2003b, *MNRAS*, 339, 312
- Springel, V., White, M., & Hernquist, L. 2001, *ApJ*, 549, 681
- Springel, V., White, S. D. M., Jenkins, A., et al. 2005c, *Nature*, 435, 629
- Steinmetz, M., & Navarro, J. F. 1999, *ApJ*, 513, 555
- Stinson, G., Seth, A., Katz, N., et al. 2006, *MNRAS*, 373, 1074
- Stinson, G. S., Brook, C., Macciò, A. V., et al. 2013, *MNRAS*, 428, 129
- Tassis, K., Kravtsov, A. V., & Gnedin, N. Y. 2008, *ApJ*, 672, 888
- Tepper-García, T., Richter, P., Schaye, J., et al. 2012, *MNRAS*, 425, 1640
- . 2011, *MNRAS*, 413, 190
- Teyssier, R. 2002, *A&A*, 385, 337
- Teyssier, R., Pires, S., Prunet, S., et al. 2009, *A&A*, 497, 335
- Thacker, R. J., & Couchman, H. M. P. 2000, *ApJ*, 545, 728
- Thacker, R. J., Scannapieco, E., & Couchman, H. M. P. 2006, *ApJ*, 653, 86
- Thielemann, F.-K., Nomoto, K., & Yokoi, K. 1986, *A&A*, 158, 17
- Torrey, P., Vogelsberger, M., Sijacki, D., Springel, V., & Hernquist, L. 2012, *MNRAS*, 427, 2224
- Tuffs, R. J., Popescu, C. C., Völk, H. J., Kylafis, N. D., & Dopita, M. A. 2004, *A&A*, 419, 821
- Tully, R. B., & Fisher, J. R. 1977, *A&A*, 54, 661
- Uhlir, M., Pfrommer, C., Sharma, M., et al. 2012, *MNRAS*, 423, 2374
- Vale, A., & Ostriker, J. P. 2004, *MNRAS*, 353, 189
- van de Voort, F., & Schaye, J. 2012, *MNRAS*, 423, 2991
- van de Voort, F., Schaye, J., Altay, G., & Theuns, T. 2012, *MNRAS*, 421, 2809
- van de Voort, F., Schaye, J., Booth, C. M., Haas, M. R., & Dalla Vecchia, C. 2011, *MNRAS*, 414, 2458
- van den Bosch, F. C. 2000, *ApJ*, 530, 177
- . 2002, *MNRAS*, 332, 456
- van der Burg, R. F. J., Hildebrandt, H., & Erben, T. 2010, *A&A*, 523, A74
- Vergani, D., Epinat, B., Contini, T., et al. 2012, *A&A*, 546, A118
- Villar, V., Gallego, J., Pérez-González, P. G., et al. 2008, *ApJ*, 677, 169
- Vogelsberger, M., Genel, S., Sijacki, D., et al. 2013, *ArXiv e-prints*, 1305.2913
- Vogelsberger, M., Sijacki, D., Kereš, D., Springel, V., & Hernquist, L. 2012, *MNRAS*, 425, 3024
- Weinberg, D. H., Hernquist, L., & Katz, N. 1997, *ApJ*, 477, 8
- Weinmann, S. M., Pasquali, A., Oppenheimer, B. D., et al. 2012, *MNRAS*, 426, 2797
- Whitaker, K. E., van Dokkum, P. G., Brammer, G., & Franx, M. 2012, *ApJ*, 754, L29
- White, S. D. M., & Frenk, C. S. 1991, *ApJ*, 379, 52
- Yoshida, M., Shimasaku, K., Kashikawa, N., et al. 2006, *ApJ*, 653, 988
- Younger, J. D., Hopkins, P. F., Cox, T. J., & Hernquist, L. 2008, *ApJ*, 686, 815
- Zahid, H. J., Dima, G. I., Kewley, L. J., Erb, D. K., & Davé, R. 2012, *ApJ*, 757, 54
- Zheng, X. Z., Dole, H., Bell, E. F., et al. 2007, *ApJ*, 670, 301
- Zibetti, S., White, S. D. M., Schneider, D. P., & Brinkmann, J. 2005, *MNRAS*, 358, 949